УДК: 517.9+532.3+534.14+519.622
MSC 2010: 34C15, 76D99, 37E99

Plate falling in a fluid: Regular and chaotic dynamics of finite-dimensional models

Sergey P. Kuznetsov

Kotel'nikov's Institute of Radio Engineering and Electronics of RAS, Saratov Branch,
410019 Saratov, Zelenaya 38, Russian Federation

Results are reviewed relating to the planar problem for falling plate in resisting medium studied with models based on ordinary differential equations for a small number of dynamical variables. A unified model is introduced to conduct a comparative analysis of dynamic behaviors of models of Kozlov, Tanabe – Kaneko, Belmonte – Eisenberg – Moses and Andersen – Pesavento – Wang using common dimensionless variables and parameters. It is shown that the overall structure of the parameter spaces for the different models shows certain similarities caused by the same inherent symmetry and by universal nature of the involved phenomena of nonlinear dynamics (fixed points, limit cycles, attractors, bifurcations).

UDK: 517.9+532.3+534.14+519.622
MSC 2010: 34C15, 76D99, 37E99

Keywords: body motion in fluid, oscillations, autorotation, flutter, attractor, bifurcation, chaos, Lyapunov exponent

---

This work was partially supported by a grant of the President of the Russian Federation for leading scientific schools NSH-1726.2014.2 "Fundamental problems of nonlinear dynamics and their applications" and RFBR grant 14-02-00085

---

spkuz@yandex.ru

Kotelnikov's Institute of Radio-Engineering and Electronics of Russian Academy of Sciences,
Saratov Branch, Zelenaya 38, Saratov, 410019, Russian Federation

Introduction

Dynamics of falling flat sheet in a resisting medium is the content of one of classical problems in hydrodynamics and aerodynamics, the analysis of which goes back to Maxwell, Kelvin, Kirchhoff, Joukovsky, relating to the XIX and early XX century [1-6].

Elementary experiments show that various kinds of dynamical behavior can occur depending on parameters and initial conditions:

- simple steady fall,
- shaking from side to side, which can be regular or irregular (flutter),
- tumbling (autorotation), regular or irregular.

Naturally, there is a problem to find conditions for implementation of these regimes, to understand their nature in the context of the theory of dynamical systems, to explore bifurcations, leading to occurrence of certain types of motion, etc.

Full and correct approach to description of motion of a body in viscous incompressible fluid implies investigation of the time-varying velocity field in the surrounding area based on the Navier – Stokes equations [7-12], which requires a complicated resource-intensive computations. Data obtained in this way are obviously not easy for comprehension, and, given the expected diversity of types of dynamics depending on many parameters still have need of qualitative interpretation of the physical level for their understanding.

A reasonable initial step to simplify the analysis is to restrict the consideration with the plane problem. It means that only two spatial coordinates X and Y are significant while the third

one Z is regarded as irrelevant: the system is assumed to be extended in Z-direction; there are no motions along this axis and no dependences of variables on Z.

Next, one can turn to approximate description of the problem with models in a form of ordinary differential equations for a small number of variables, i.e., to dynamical systems with a relatively small dimension of the phase space. Although validity of such approach is not so obvious, it has a grate advantage that within this framework one can involve powerful conceptual tools of modern dynamical systems theory for the analysis of the problem. In particular, such well-established and proven methodology of computational studies and data processing like graphical presentation of portraits of attractors [13-15], charts of dynamical regimes in the parameter space [15-17], computation of Lyapunov exponents [18,14,15], bifurcation analysis [19] may be applied in the explorations.

A foundation for legitimate finite-dimensional description is the fact that governing equations for generalized coordinates and velocities of the solid body moving in ideal non-viscous incompressible fluid can be separated from the field equations of the fluid itself. The corresponding equations were derived and studied in due time by Kirchhoff [2, 7-10, 20, 21]. Effect of fluid motion on the body only modifies the inertial properties; instead of usual masses and moments of inertia, one has to deal in the equations with added masses and moments of inertia due to the contribution of the fluid motions in adjacent space regions. In the plane problem forces on the body from the fluid are determined by circulation of the velocity field around the body profile, and in the case of ideal fluid the circulation appears simply as a constant parameter; in particular, it may be zero.

Actually the Kirchhoff equations relate to a situation of excluded losses of mechanical energy, and the corresponding dynamical system is conservative. Then, many properties of the falling body dynamic behavior significant from the practical point of view remain outside the scope of the consideration as they are associated with dissipation. It relates e.g. to steady fall regimes and to sustained regular or chaotic oscillations and rotations [20, 21]. To account and study such motions it seems natural to account dissipation in a phenomenological way by means of appropriately chosen additional terms to the Kirchhoff equations [22-28].

This review is devoted to models for the plane hydrodynamic problem based on ordinary differential equations and to mutual comparison of these models. One of the main goals is to fulfill the picture of dynamical phenomena relating to this problem with concrete content and illustrative material obtained in computations. Relationship of this material with results based on the Navier – Stokes equations [29-32], as well as with experimental data [33-38], will not be concerned. Also we do not discuss situations of motion of bodies in resisting media beyond the plane problem [36-38] and generalizations, including control of the body motion in fluid [39-43].

In Section 1 we discuss the plane problem of the fall of the body of elliptic profile in ideal fluid, and equations of motion are presented accounting the effect of added masses. Section 2 is devoted to a special case where the gravity is compensated by the buoyancy force, and the dynamics is reduced to a pendulum-type equation with sinus-function nonlinearity. In Section 3 we consider a Kozlov model derived from a conservative system with taking into account only the viscous friction forces and the torque resistance force linear in the generalized velocities. A special case is discussed when the model is integrable and reduces to the pendulum equation with damping, and analysis of stability loss for a steady uniform fall is examined that may lead to arising autorotation. In Section 4 a modification of the model is considered, in which the gravity is excluded, constant circulation is assumed, and constant torque of external force is applied to the body. It is shown that in this situation the chaotic dynamics occurs associated with the strange attractor of Lorenz type. Section 5 is devoted to a model introduced by Tanabe and Kaneko, which takes into account the forces of resistance and lift due to presence of circulation, expressed via the dynamical variables using the postulate of Kutta – Joukovsky – Chaplygin. Accounting critical remarks in address of this model in the literature, we consider ways of its modification to account for them. Approximate analysis of a non-standard bifurcation accompanying transition from the steady fall to the oscillatory regime in the Tanabe – Kaneko

model is developed. Section 6 discusses the model advanced by Belmonte, Eisenberg and Moses, in which, unlike the Tanabe – Kaneko model, the resistance force and torque depend quadratically on the generalized velocities. In Section 7 we consider a model elaborated by Andersen, Pesavento, and Wang who introduce empirically chosen dissipative terms in the Kirchhoff equations on a base of fitting the data of numerical solution of the Navier – Stokes equations. In Section 8 generalized equations are formulated to allow using one and the same set of dimensionless variables and parameters for comparative analysis of the dynamic behavior of all the mentioned models.

1. Plane problem of the body fall in ideal fluid

We will use two coordinate systems: the laboratory frame (X, Y), where a position of the center of mass of the body is given by the Cartesian coordinates X and Y, and the moving frame (x, y), the axes of which are fixed relative to the body (Figure 1).

Let us start with the problem of body fall in ideal incompressible non-viscous fluid.

Taking into account inertial properties of the body and its environment, the kinetic energy may be written in the form

$$T = \tfrac{1}{2}(m + m_x)v_x^2 + \tfrac{1}{2}(m + m_y)v_y^2 + \tfrac{1}{2}(I + J)\dot{\theta}^2, \tag{1.1}$$

where v_x and v_y are velocity components in the moving frame, $\dot{\theta}$ is the angular velocity, the time derivative of the angular coordinate of the body, m is the mass and I is the moment of inertia of the body. The additives m_x, m_y, and J account the added masses due to involvement of surrounding fluid volumes in the motion. We assume that the body is of density ρ_s, and the fluid is of density ρ_f. As we deal with the plane problem the densities are defined as mass per unit area in a cross section.

According to classic hydrodynamics [7-12], for a body moving in ideal non-viscous fluid the resistance forces are absent (the d'Alembert – Euler paradox), but forces acting on the body appear due to non-zero circulation Γ of the velocity field around a contour enclosing the body (Joukovsky theorem). The value of Γ does not depend on particular choice of the contour. Moreover, Γ remains constant in time (the Kelvin – Helmholtz theorem) been determined by initial conditions for the velocity field in the fluid. The components of the force are $f_x = -\rho_f \Gamma v_y$ and $f_y = \rho_f \Gamma v_x$.

In presence of gravity characterized by the gravitational acceleration g reduced due to the buoyancy, the equation for the velocity components and the angular variable read

$$\begin{aligned}
&(m + m_x)\dot{v}_x = (m + m_y)v_y\dot{\theta} - \rho_f \Gamma v_y - mg(1 - \rho_f \rho_s^{-1})\sin\theta,\\
&(m + m_y)\dot{v}_y = -(m + m_x)v_x\dot{\theta} + \rho_f \Gamma v_x - mg(1 - \rho_f \rho_s^{-1})\cos\theta,\\
&(I + J)\ddot{\theta} = (m_x - m_y)v_x v_y.
\end{aligned} \tag{1.2}$$

The coordinates of the center of mass in the laboratory frame evolve in time as determined by the differential equations

$$\dot{X} = v_x\cos\theta - v_y\sin\theta, \;\; \dot{Y} = v_x\sin\theta + v_y\cos\theta. \tag{1.3}$$

For the body of elliptic profile with semiaxes a and b the mass and the moment of inertia are

$$m = \pi\rho_s ab, \; I = \tfrac{1}{4}\pi\rho_s ab(a^2 + b^2); \tag{1.4}$$

the added masses and moment of inertia in ideal non-viscous fluid are expressed as [9]

$$m_x = \pi\rho_f b^2, \; m_y = \pi\rho_f a^2, \;\; J = \tfrac{1}{8}\pi\rho_f (a^2 - b^2)^2. \tag{1.5}$$

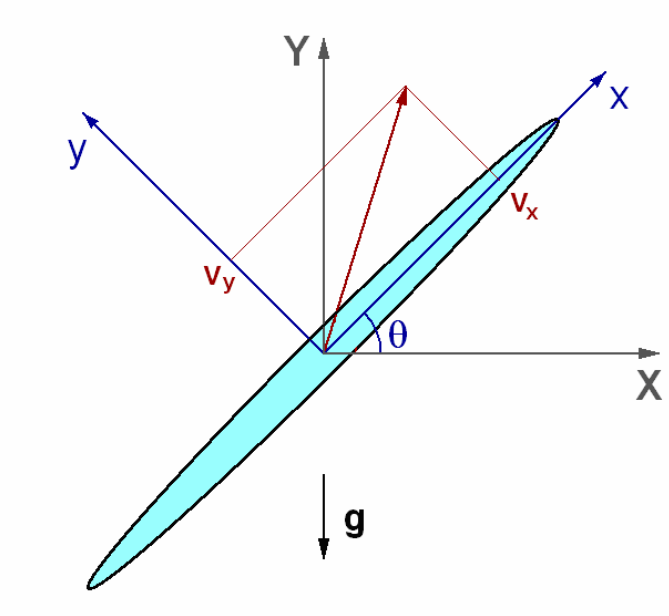

Figure 1: Laboratory and moving coordinate frames in the plane problem of the body fall in a resisting medium

Substitution of these relations in (1.2) yields

$$\begin{aligned} A\dot{v}_x &= Bv_y\dot{\theta} - \rho\beta^{-1}\frac{\Gamma v_y}{\pi a^2} - g(1-\rho)\sin\theta, \\ B\dot{v}_y &= -Av_x\dot{\theta} + \rho\beta^{-1}\frac{\Gamma v_x}{\pi a^2} - g(1-\rho)\cos\theta, \\ Q\ddot{\theta} &= a^{-2}(A-B)v_x v_y, \end{aligned} \tag{1.6}$$

where shortened notation for the coefficients is used:

$$A = 1+\rho\beta,\ B = 1+\rho\beta^{-1},\ Q = \tfrac{1}{4}(1+\beta^2) + \tfrac{1}{8}\rho\beta^{-1}(1-\beta^2)^2. \tag{1.7}$$

Here $\rho = \rho_f / \rho_s$ is the ratio of densities for the fluid and the body, and $\beta = b/a$ is the ratio of the semiaxes of the ellipse.

In some cases it is convenient additionally to normalize the velocity components as $u = v_x / a,\ \ v = v_y / a$ and rewrite the equations (1.6) in the form

$$\begin{aligned} A\dot{u} &= Bv\dot{\theta} - \rho\beta^{-1}\frac{\Gamma v}{\pi a^2} - ga^{-1}(1-\rho)\sin\theta, \\ B\dot{v} &= -Au\dot{\theta} + \rho\beta^{-1}\frac{\Gamma u}{\pi a^2} - ga^{-1}(1-\rho)\cos\theta, \\ Q\ddot{\theta} &= (A-B)uv. \end{aligned} \tag{1.8}$$

2. Conservative dynamics without gravity

Consider first the case of equal density of the fluid and the body, ρ=1. Then the gravity effect is excluded by the buoyancy, and equations (1.8) take the form

$$\begin{aligned} A\dot{u} &= Bv\dot{\theta} - \Gamma' v, \\ B\dot{v} &= -Au\dot{\theta} + \Gamma' u, \\ Q\ddot{\theta} &= (A-B)uv, \end{aligned} \tag{2.1}$$

where $\Gamma' = \Gamma / \pi a^2\beta = \Gamma / \pi ab$. The substitution

$$u = RA^{-1}\cos\varphi,\ v = -RB^{-1}\sin\varphi \tag{2.2}$$

transforms the equations to

$$\begin{aligned}
&\dot{R} = \Gamma' R\frac{A-B}{AB}\sin\varphi\cos\varphi,\\
&\dot{\varphi} = \dot{\theta} - \Gamma'(A^{-1}\cos^2\varphi + B^{-1}\sin^2\varphi),\\
&\ddot{\theta} = -\frac{A-B}{ABQ}R^2\sin\varphi\cos\varphi.
\end{aligned} \tag{2.3}$$

Here φ is an instant angle between the principal axis of the elliptic profile and the translational velocity of the body, and θ is an instant angle of inclination of the principal axis of the elliptic profile measured in the laboratory frame.

If we multiply the first equation by R and compose a sum with the third equation, the right-hand part vanishes, and a combination under the derivative is then an integral of motion:

$$D^2 = R^2 + 2\Gamma' Q\dot{\theta} = \text{const}. \tag{2.4}$$

Expressing R from this relation we obtain a single equation for the angular variable φ:

$$\ddot{\varphi} = \frac{A-B}{2QAB}\left(-D^2 + \Gamma'^2 Q\frac{A+B}{2AB} - \Gamma'^2 Q\frac{A-B}{2AB}\cos 2\varphi\right)\sin 2\varphi. \tag{2.5}$$

In the case of zero circulation $\Gamma' = 0$ the equations (2.1) for the variables u, v, $w = \dot{\theta}$ take the form [7]

$$A\dot{u} = Bvw,\ B\dot{v} = -Auw,\ Q\dot{w} = (A-B)uv. \tag{2.6}$$

According to (2.4), the integral of motion in this case is R and it corresponds to conservation of translational momentum of the body with account of the added masses. From the second equation (2.3) we see that $\dot{\varphi} = \dot{\theta}$, so without loss of generality, in this case one can identify φ and θ. (This is so because an origin for θ can be chosen arbitrarily due to spatial isotropy of the problem without gravity.) Then, for θ we get the relation

$$\ddot{\theta} + \frac{(A-B)}{ABQ}R^2\cos\theta\sin\theta = 0, \tag{2.7}$$

which coincides precisely with the pendulum equation written for the doubled angular variable $\vartheta = 2\theta$ (due to the identity $\sin\theta\cos\theta = \frac{1}{2}\sin 2\theta$) [7]. Figure 2 shows the phase portrait for this equation in the plane $(\theta, \dot{\theta})$. Due to the fact that θ is a cyclic variable, the configuration is 2π-periodic. Therefore, the phase portrait can be thought as placed on a surface of a cylinder resulting from rolling a plane band of width 2π into a tube and gluing the vertical edges together.

The fixed points $\theta = \pi/2$ and $\theta = 3\pi/2$ are stable centers corresponding to the uniform motion of the body, wide side forward. The fixed points $\theta = 0$ and $\theta = \pi$ represent unstable saddle states corresponding to the uniform motion of the profile, edge forward. On the phase portrait one can see the separatrix containing the saddle points. Orbits inside the separatrix correspond to oscillatory motions around the centers, while the rotational motions are represented by curves outside the separatrix. Motion precisely on the separatrix can be obtained setting the initial conditions $\theta_0 = \frac{\pi}{2}$, $w_0 = \pm R\sqrt{\frac{B-A}{ABQ}}$.

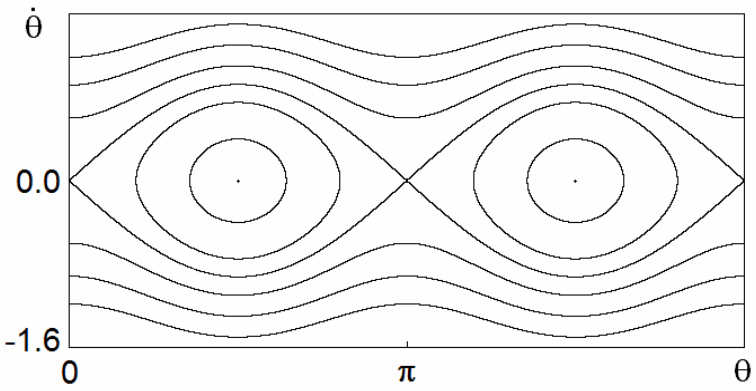

Figure 2. Phase portrait of the equation (2.7) with $\beta = 0.25, R = 1$

Diagrams in Figure 3 illustrate motions of the body in real space as obtained from joint numerical integration of equations (2.6) and equations for coordinates of the center of mass: $\dot{X} = u\cos\theta - v\sin\theta$, $\dot{Y} = u\sin\theta + v\cos\theta$. The top picture relates to a stable steady motion of the body associated with the fixed point of center on the phase portrait. Further, from top to down, there are illustrations for the oscillatory side to side motion, the motion along the separatrix asymptotically approaching an unstable stationary state, and rotation, when the body tumbles in the course of time evolution.

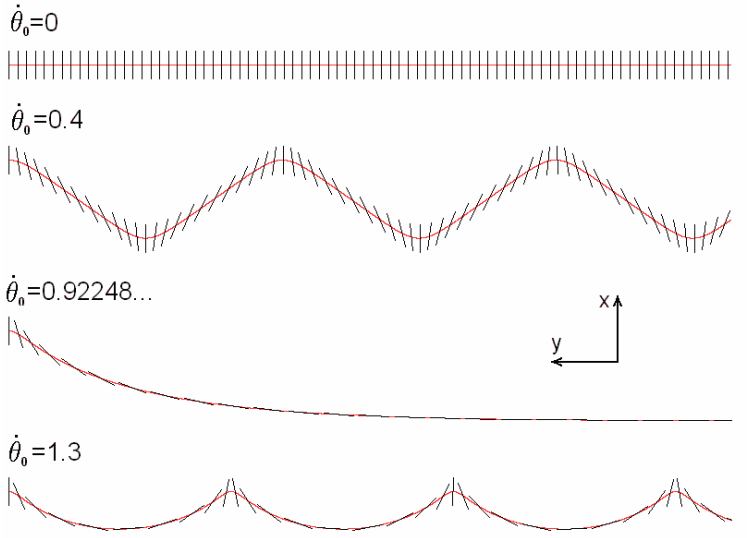

Figure 3. Motion of the body of elliptic profile in ideal fluid without circulation at β=0.25, *R*=1. Positions of the principal axis are shown at successive time instants. The initial angle is $\theta_0 = \pi/2$,and initial angular velocities are listed in the inscriptions

In presence of non-zero circulation, the variables φ (the angle between the velocity vector and the principal axis of the ellipse) and θ (the angle of inclination of the profile in the laboratory frame) must be distinguished as they behave differently. Fig. 4 shows the phase portrait at the value of the integral of motion *D*=1 and circulation Γ=0.4 on the plane of variables φ and $w = \dot{\theta}$. Although the form of trajectories differs from that of Figure 2, the topological structure remains the same. Observe again the fixed points, the stable centers, and the unstable saddles, located at the separatrix subdividing the plane onto regions of oscillatory motions represented by closed curves and regions of rotational motions associated with curves going from side to side of the rectangle. Analysis of motions in space in the case of non-zero circulation shows that the oscillatory or rotational motions of the body take place on a background of a gradual displacement of the center of mass around some midpoint (Figure 5).

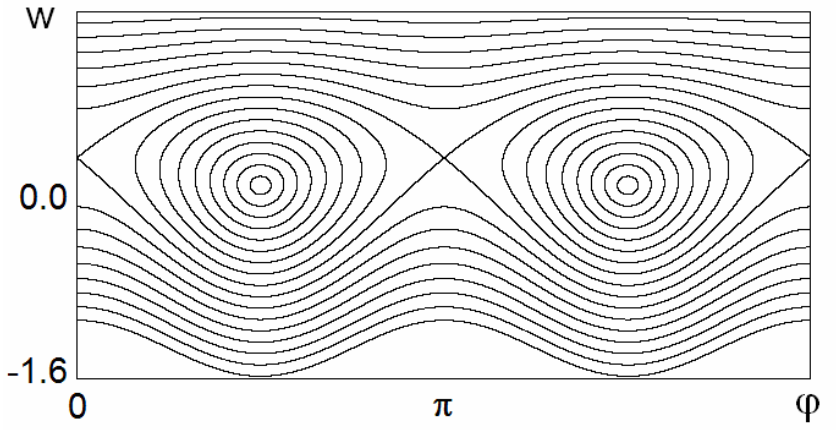

Figure 4: Phase portrait of the dynamics in the case of non-zero circulation, $\Gamma = 0.4$, $\beta = 0.25$, $D = 1$.

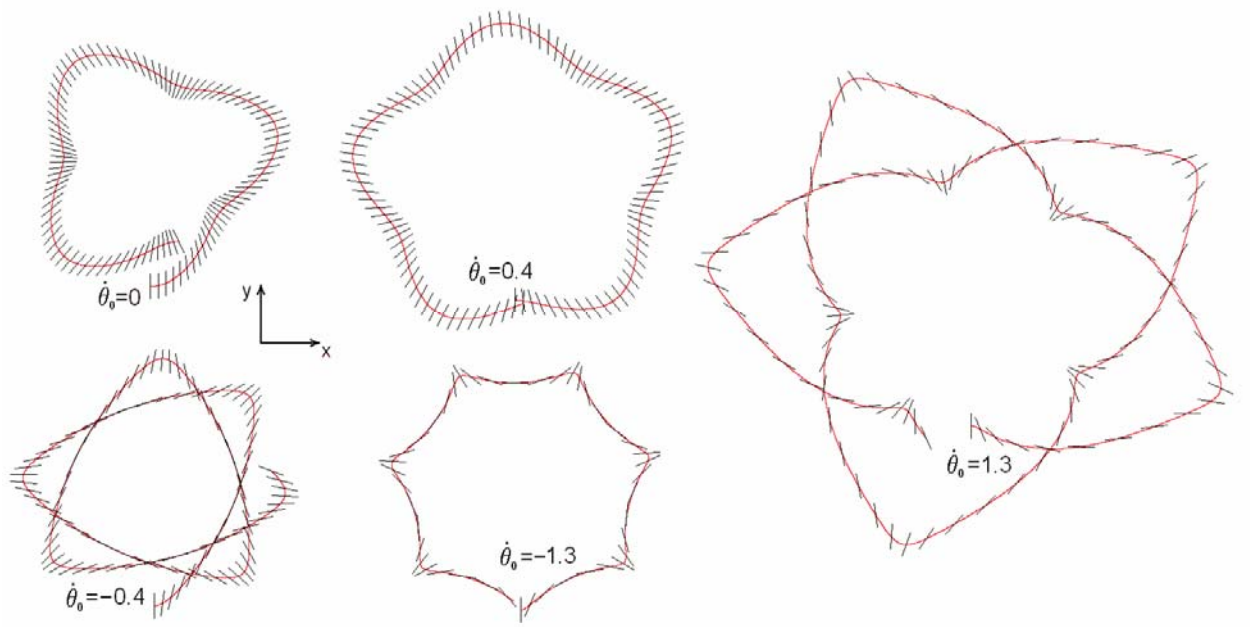

Figure 5: Diagrams illustrating the motion of the body of elliptical profile in ideal fluid for the case of non-zero circulation $\Gamma=1$ for $\beta = 0.25$ with different initial conditions.

The above quite simple and descriptive results provide a good starting point for further analysis of motions in the presence of dissipation and gravity. It is analogous to a productive approach in theory of oscillations, when a conservative oscillator is considered as a paradigmatic model for subsequent modifications involving say, damping oscillations or self-oscillations corresponding to attracting closed orbits, the limit cycles [44,45].

For systems whose states are represented on the phase cylinder, the oscillation theory distinguishes the limit cycles of the first kind as closed loops on the cylinder surface, and of the second kind, as the curves bypassing around the cylinder. In the context of the problem of the body fall in fluid, the first case will correspond to oscillations from side to side (flutter), and the second to the fall with tumbling (autorotation).

3. Kozlov model: Falling body with viscous friction

The simplest model of the body fall in fluid with gravity and viscous friction is based on suggestion that the circulation is zero, and the added dissipative terms are proportional to the translation velocity components and to the angular velocity [22].

When taking into account the viscous friction, it seems natural to depart from the well-known Stokes formula [7, 9-11]. For steady motion of a sphere of radius R_0 in viscous medium with velocity V it reads

$$F = -6\pi\eta R_0 V\,, \tag{3.1}$$

where η is the viscosity coefficient. It is useful in many cases to represent it as a product of the fluid density and the kinematical viscosity: $\eta = \rho_f \nu$. For the body in the form of an ellipsoid with semi-axes *a*, *b*, *c* there is a generalization [7], the same formula, but with modified geometric parameter R_*. In the case of motions along the *a*-axis it is

$$\frac{1}{R_*} = \int_0^\infty \frac{3(\lambda + 2a^2)d\lambda}{8\sqrt{(\lambda + a^2)^3(\lambda + b^2)(\lambda + c^2)}}\,. \tag{3.2}$$

In the context of three-dimensional problem of the fall in the fluid this solution could be used for bodies in the form of "pancake" (disc of elliptical shape) in a limit case of high viscosity. However, in a rigorous two-dimensional formulation it is not applicable according to the so-called Stokes paradox [7, 10, 11]. Nevertheless, from the physical point of view, since in reality the geometric dimensions of the body are limited in all three dimensions, it seems appropriate to assume that the components of the viscous force are represented by expressions similar in structure to the Stokes formula, namely, as

$$F_x = -c_1\eta a v_x,\; F_y = -c_2\eta a v_y\,, \tag{3.3}$$

and the viscous resisting torque for rotational motion is

$$M_\theta = -c_3\eta a^3\dot\theta\,, \tag{3.4}$$

where $c_{1,2,3}$ are some coefficients. Taking these forces into account corresponds to adding terms in (1.8) being the derivatives of the Rayleigh function [22]

$$R = \tfrac{1}{2}c_1\eta a v_x^2 + \tfrac{1}{2}c_2\eta a v_y^2 + \tfrac{1}{2}c_3\eta a^3\dot\theta^2 \tag{3.5}$$

over the respective generalized velocities. Then, instead the equations (1.8) we write

$$\begin{aligned} A\dot u &= -\mu_1 u + Bv\dot\theta - P\sin\theta,\\ B\dot v &= -\mu_2 v - Au\dot\theta - P\cos\theta,\\ Q\ddot\theta &= -\mu_3\dot\theta + (A-B)uv, \end{aligned} \tag{3.6}$$

where $\mu_{1,2,3} = \eta\beta^{-1}\pi^{-1}a^{-1}c_{1,2,3} = \rho\beta^{-1}\pi^{-1}\nu a^{-1}c_{1,2,3} = \rho\beta^{-1}k_{1,2,3}$, $P = ga^{-1}(1-\rho)$.

If the ratio of the friction coefficients for motions along two principal axes of the elliptical profile is equal to the ratio of the effective masses, the equation (3.6) can be integrated analytically. Indeed, let $\mu_1 = A\mu$, $\mu_2 = B\mu$, and $z = (Au + iBv)e^{-\mu t - i\theta}$. Then, from the first two equations (3.6) we obtain $\dot z = -iPe^{\mu t}$ and $z = -iP\int e^{\mu t}dt$. Thus, we have

$$\begin{aligned} Au &= -P\mu^{-1}(1-e^{-\mu t})\sin\theta + ce^{-\mu t}\sin(\theta+\alpha),\\ Bv &= -P\mu^{-1}(1-e^{-\mu t})\cos\theta + ce^{-\mu t}\cos(\theta+\alpha), \end{aligned} \tag{3.7}$$

where *c* and α are constants determined by initial conditions. At asymptotically large *t* the velocities satisfy the relations

$$u = -PA^{-1}\mu^{-1}\cos\theta,\quad v = -PB^{-1}\mu^{-1}\sin\theta. \tag{3.8}$$

The angular variable in this asymptotic regime will be governed by the third equation of (3.6), where one has to substitute (3.8). Then, it takes a form of the damped pendulum equation

$$\ddot\theta = -\frac{\mu_3}{Q}\dot\theta + \frac{(A-B)P^2}{QAB\mu^2}\sin\theta\cos\theta\,. \tag{3.9}$$

(Note an obvious correspondence of it to equation (2.3) for the conservative case.) If the initial conditions are selected in such way that the body motion was originally rotational, then over time it transforms, first, to oscillation without tumbling, and then the oscillations decay, and finally the steady fall occurs, which corresponds to a stable fixed point

$$u = 0,\ v = -P/\mu_2,\ w = \dot{\theta} = 0,\ \theta = 0\,. \tag{3.10}$$

(One more stationary solution $\theta=\pi$ is equivalent in properties to (3.13), as there are two orientations of the body in the fall, one or other wide side down.)

Kozlov also studied stability of the stationary solutions of (3.10) for arbitrary friction coefficients $\mu_{1,2,3}$. Let us add small perturbations to the solution (3.10), then, in the first order we obtain from (3.5) the following equations for the perturbations marked with a tilde:

$$\begin{aligned} A\dot{\tilde{u}} &= -\mu_1\tilde{u} - BP\mu_2^{-1}\tilde{w} - P\tilde{\theta},\\ B\dot{\tilde{v}} &= -\mu_2\tilde{v},\\ Q\dot{\tilde{w}} &= -\mu_3\tilde{w} + (B-A)P\mu_2^{-1}\tilde{u}\\ \dot{\tilde{\theta}} &= \tilde{w}. \end{aligned} \tag{3.11}$$

The exponential substitution $\tilde{u},\tilde{v},\tilde{w},\tilde{\theta} \sim e^{st}$ yields the characteristic equation

$$\left(s+\frac{\mu_2}{B}\right)\left[s^3 + \left(\frac{\mu_1}{A}+\frac{\mu_3}{Q}\right)s^2 + \frac{\mu_1\mu_2^2\mu_3 + (B-A)BP^2}{\mu_2^2AQ}s + \frac{(B-A)P^2}{\mu_2AQ}\right] = 0\,. \tag{3.12}$$

Among four roots of this equation, there is a trivial one, $s_0 = -\mu_2/B$, and the remaining three roots may be obtained by solving the cubic equation with real coefficients. Stability loss occurs when a real part of a pair of complex conjugate roots vanishes. This condition can be derived if we look for a solution of (3.12) in the form $s = i\varsigma$ that leads to relations

$$\left[-\varsigma^2 + \frac{\mu_1\mu_2^2\mu_3 + (B-A)BP^2}{\mu_2^2AQ}\right]\varsigma = 0,\ \ \left(\frac{\mu_1}{A}+\frac{\mu_3}{Q}\right)\varsigma^2 - \frac{(B-A)P^2}{\mu_2AQ} = 0\,. \tag{3.13}$$

Assuming $\varsigma \neq 0$ we have

$$\frac{\mu_2}{B} = \left(\frac{\mu_1}{A}+\frac{\mu_3}{Q}\right)\left[1 + \frac{\mu_1\mu_2^2\mu_3}{(B-A)BP^2}\right]. \tag{3.14}$$

(Note that in the integrable case $\mu_2/B = \mu_1/A$ the equality is impossible: while $\mu_{1,2,3} > 0$ and $B > A$, the right part in (3.14) is obviously greater than the left part, so the fixed point (3.10) is always stable.)

To pass from elliptic profile to a thin plate, it is natural to consider the limit $\beta = b/a \to 0$.[1] Meaningful the case is when simultaneously the density ratio approaches zero too, while the value $r = \rho/\beta$ remains fixed. This ratio is regarded as a relevant parameter of the model. Producing normalization of time, velocities, and friction coefficients

$$t = t'\sqrt{g^{-1}a},\ u = u'\sqrt{ga^{-1}},\ v = v'\sqrt{ga^{-1}},\ \ k_{1,2,3} = k'_{1,2,3}\sqrt{ga^{-1}}\,, \tag{3.15}$$

[1] Rigorously, this limit transition leads to a non-uniform mass distribution on the plate and decrease of the linear density from central maximum to the edges according the law $\sqrt{a^2-x^2}$. Unlike the moment of inertia $\frac{1}{3}ma^2$ of a homogeneous plate, in this limit we have $\frac{1}{4}ma^2$. However, in a frame of qualitative analysis, this difference seems not principal.

and omitting primes for brevity, we arrive at the equations

$$\begin{aligned} \dot{u} &= -rk_1 u + (1+r)v\dot{\theta} - \sin\theta, \\ (1+r)\dot{v} &= -rk_2 v - u\dot{\theta} - \cos\theta, \\ (\tfrac{1}{4}+\tfrac{1}{8}r)\ddot{\theta} &= -rk_3\dot{\theta} - ruv, \end{aligned} \qquad (3.16)$$

Equations (3.16) correspond to the form (3.6) with $A=1$, $B=1+r$, $Q=\frac{1}{4}+\frac{1}{8}r$, $P=1$, $\mu_{1,2,3}=rk_{1,2,3}$, and all the above results can be easily reformulated for them. In particular, it concerns the reduction to the pendulum equation with damping (3.9) in the integrable case with $k_1=k_2/(1+r)$. Also, the condition of stability loss for the fixed point corresponding to the steady fall (3.14) can be rewritten as

$$\frac{k_2}{1+r}=\left(k_1+\frac{8k_3}{2+r}\right)\left(1+\frac{r^3k_1k_2^2k_3}{1+r}\right). \qquad (3.17)$$

Figure 6 illustrates dynamics of the model (3.16) in the phase plane $(\theta, \dot{\theta})$ that may be interpreted as well as the phase cylinder. In diagram (a) the motion being initially rotational, transforms to damping oscillations, and eventually approaches a fixed point corresponding to the stable steady fall. In diagram (b) the trajectory departs spiraling from the unstable fixed point, and converges to a limit cycle of the second kind around the cylinder, which corresponds to the autorotation. Fig. 7 illustrates the respective spatial motions of the plate in fluid.

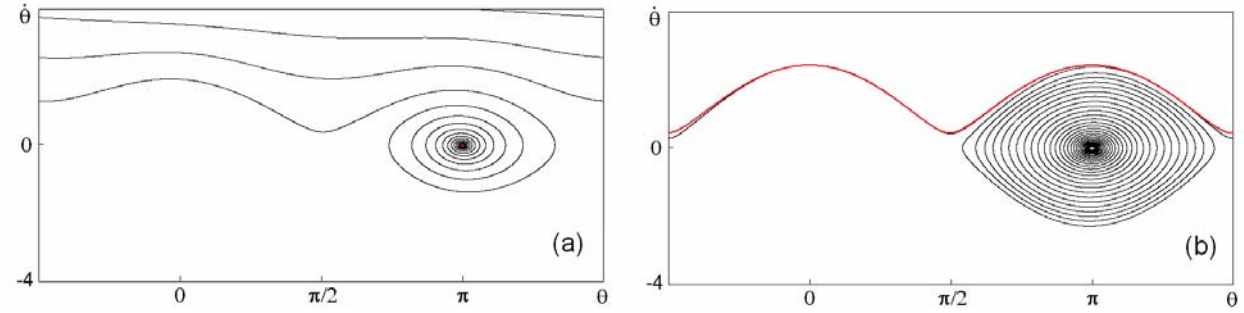

Figure 6: Phase trajectories in Kozlov model (3.16) with $r=2$, $k_2=1$, $k_3=0.04$, $k_1=\frac{1}{3}$ (a), and $k_1=\frac{1}{5}$ (b). Attractors are shown in red; this is a fixed point in panel (a) and a limit cycle of the second kind responsible for autorotation in panel (b).

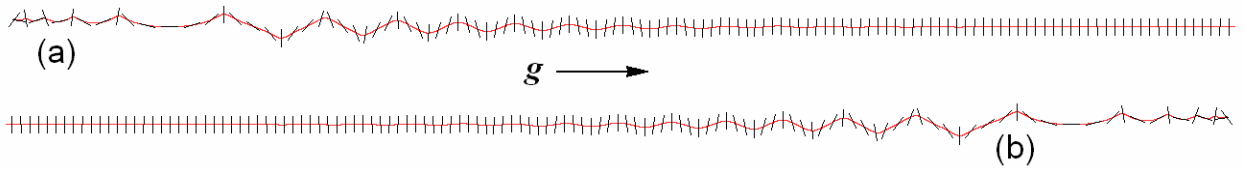

Figure 7: The spatial motion of the falling plate in the Kozlov model with parameters corresponding to panels (a) and (b) in the previous figure.

Despite simplicity of the Kozlov model, it manifests non-trivial phenomena of nonlinear dynamics, like transition to chaos through period doubling, strange attractors, and multistability in certain parameter regions (see Section 8.2).

To conclude this Section, we mention briefly the work of Mahadevan [26], where the problem formulation is similar to that of Kozlov, but with taking into account a nonlinear dependence of the resistance force on the velocity. The author defines the nonlinear friction in such a way that the drag coefficient for each component of the force depends only on the velocity component in the same direction that is hardly justified.The model takes into account a possible displacement of the center of mass of the body relative to the geometric center of the elliptic profile and a possibility of non-zero circulation around the profile, which is considered as

a constant parameter Γ. Analytical results are consistent with those of Kozlov, with the addition that the asymmetric case also is considered. Numerical results are presented in very restricted volume, and they are irreproducible because of obvious errors specifying relevant parameters in the text of the article.

4. Lorenz attractor in a model of body motion in fluid

Lorenz attractor [46-48] is a popular object of nonlinear dynamics, well studied by mathematicians. It relates to a class of quasi-hyperbolic (or singular hyperbolic) strange attractors. Chaotic dynamics on the Lorenz attractor is rigorously stated and justified [49].

Here we demonstrate that motion of a body of elliptical profile in viscous fluid may be associated with the Lorenz-type attractor.

Under assumptions of the Kozlov model (3.6), consider a case of equal densities ρ=1, when the effect of gravity is excluded (i.e. P=0), and assume presence of constant nonzero circulation Γ. Additionally, in the equation for the angular velocity we include a term of a constant external torque. So, we arrive at the equations

$$\begin{aligned} A\dot{u} &= Bvw - \Gamma v - \mu_1 u, \\ B\dot{v} &= -Auw + \Gamma u - \mu_2 v, \\ Q\dot{w} &= -(B-A)uv - \mu_3 w + M, \end{aligned} \tag{4.1}$$

where $w = \dot{\theta}$. By the change of variables and parameters

$$u = x\sqrt{A^{-1}BQ/(B-A)},\ v = y\sqrt{AB^{-1}Q/(B-A)},\ w = M\mu_3^{-1} - z, \tag{4.2}$$

$$\begin{aligned} \nu_1 &= \mu_1 A^{-1},\ h_1 = M\mu_3^{-1} - \Gamma B^{-1}, \\ \nu_2 &= \mu_2 B^{-1},\ h_2 = \Gamma A^{-1} - M\mu_3^{-1}, \\ \nu_3 &= \mu_3 Q^{-1}, \end{aligned} \tag{4.3}$$

the equations are reduced to the form similar to the Lorenz model:

$$\begin{aligned} \dot{x} &= h_1 y - \nu_1 x - yz, \\ \dot{y} &= h_2 x - \nu_2 y + xz, \\ \dot{z} &= -\nu_3 z + xy. \end{aligned} \tag{4.4}$$

In the case $h_1 = h_2$ they coincide exactly with equations for parametric excitation of waves considered by Pikovsky, Rabinovich and Trahtengerts [50] who demonstrated the Lorenz type attractor, e.g. at $\nu_1 = 1,\ \nu_2 = 4,\ \nu_3 = 1,\ h = 5.875$.

Having taken arbitrarily β=0.25 and, respectively, $A = 1+\beta = 1.25$, $B = 1+\beta^{-1} = 5$, $Q = \frac{1}{4}(1+\beta^2) + \frac{1}{8}\beta^{-1}(1-\beta^2)^2 = 0.705$, we obtain from (4.3)

$$\mu_1 = 1.25,\ \mu_2 = 20,\ \mu_3 = 0.705,\ M = 6.903,\ \Gamma = 19.583. \tag{4.5}$$

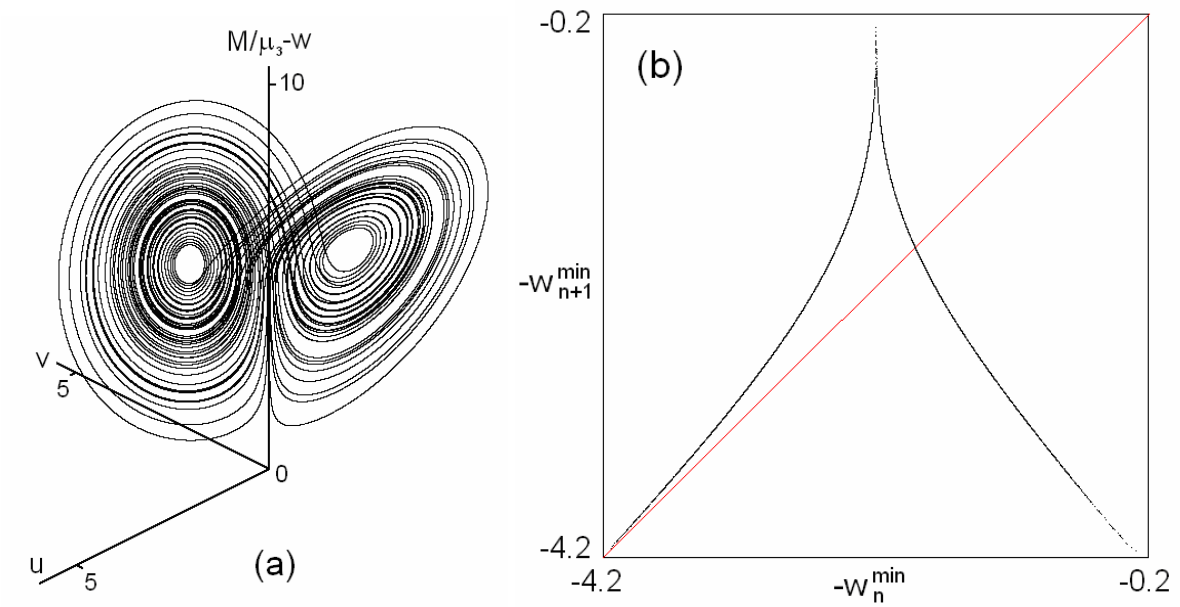

Figure 8: Lorenz-type attractor in three-dimensional states space (a) and plot of the map for consecutive minima of the variable w in the course of time evolution (b). The diagrams are based on data of numerical solution of equations (4.1) with $\mu_1 = 1.25$, $\mu_2 = 20$, $\mu_3 = 0.705$, $M = 6.903$, $\Gamma = 19.583$.

Figure 8 shows a three-dimensional portrait of the attractor in the phase space of the system (4.1) obtained from numerical solution of the equations with these parameters and a plot for the map prepared according to the procedure proposed in the original paper of Lorenz, where successive minima of the variable w achieved during the temporal evolution of the system are plotted. Observe the characteristic form with a sharp maximum, resembling a classic "saw tooth" map [46, 47, 50, 14, 15] that supports the quasi-hyperbolic nature of the attractor similar to the classic Lorenz attractor.

Figure 9 provides portraits of the attractor in the planes of variables u, v and $\varphi = \arg(u + iv)$, $w = \dot{\theta}$, which can be compared with the diagrams for other models discussed in this review. From the diagram (b) it is clear that the dynamics must be interpreted as a chaotic rotation.

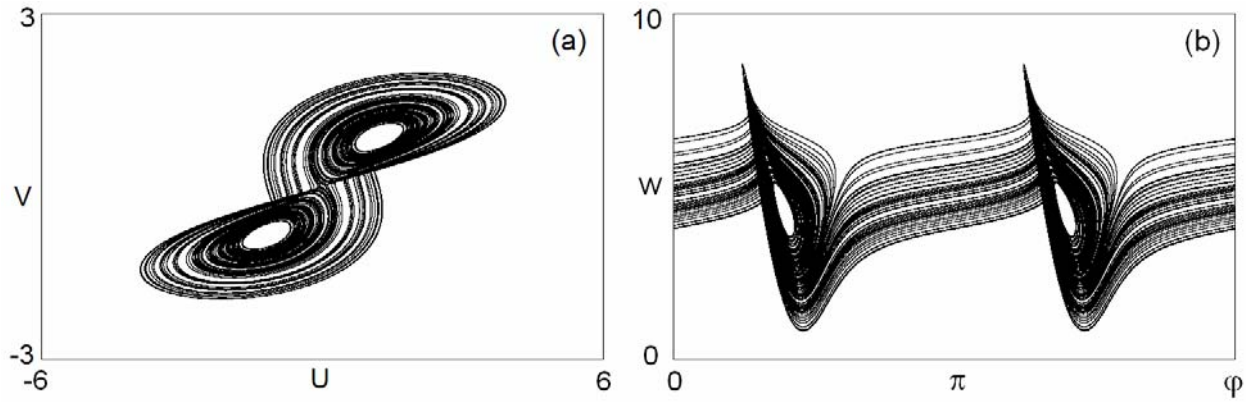

Figure 9: Attractor of the system (4.1) in projection on the planes of variables (u, v) and (φ, w). Parameters are the same as those in figure 8. The fact that the trajectories are crossing the borders of the rectangle in the diagram (b), i.e. go around the phase cylinder, indicates the presence of rotational (tumbling) motion of the body.

Figure 10 illustrates the real space-time motion of the body associated with dynamics on the Lorenz attractor in the subspace of the generalized velocities. To draw this diagram, the numerical solution of the equations (4.1) is carried out together with the equations for the angular velocity and for the coordinates of the center of mass

$$\dot{\theta} = w, \quad \dot{X} = u\cos\theta - v\sin\theta, \quad \dot{Y} = u\sin\theta + v\cos\theta\,. \tag{4.6}$$

The figure shows that the motion is accompanied by chaotic oscillations and tumbling of the body according to the chaotic nature of the attractor.

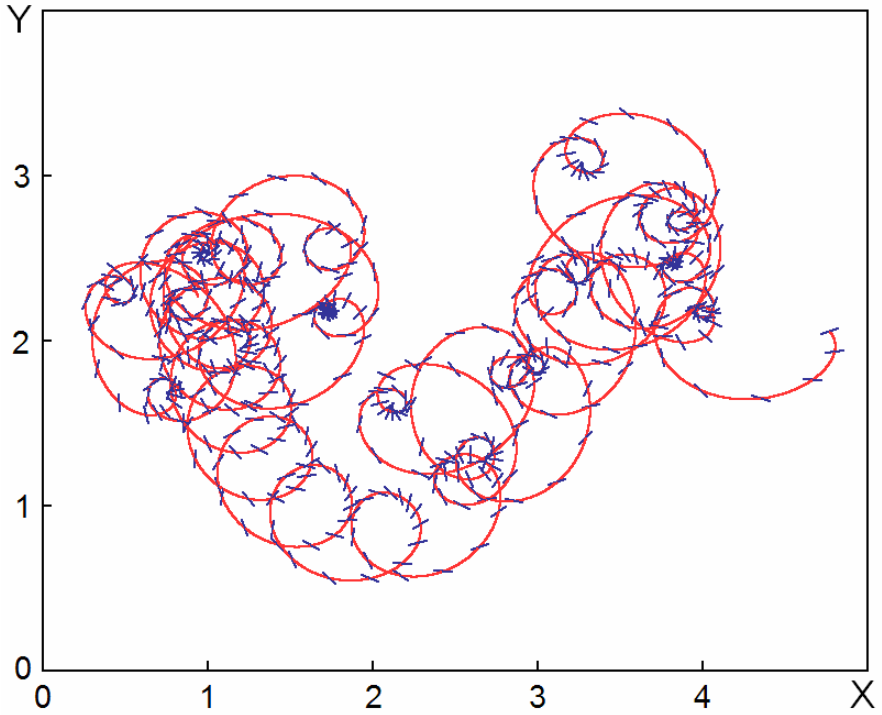

Figure 10: Spatial motion of the body in a situation where the Lorenz attractor holds in the space of generalized velocities (u, v, w). Parameters are the same as those in figure 8.

To quantify characteristics of chaos it is appropriate to use the Lyapunov exponents. Full spectrum of Lyapunov exponents of the system (4.1), (4.6) has three zero members corresponding to perturbations of center of mass shift along two coordinate axes and of variation of the angle inclination. Beside them, there are three non-trivial exponents relating to the Lorenz attractor of the subsystem (4.1). Their computation from simultaneous numerical solution of equations (4.1) and the corresponding variation equations with the Benettin algorithm [18, 15] yields

$$\lambda_1 = 0.390 \pm 0.003,\ \lambda_2 = -0.0002 \pm 0.0007,\ \lambda_3 = -6.390 \pm 0.003\,. \qquad (4.6)$$

Presence of the positive exponent in this list (4.6) indicates occurrence of chaos, characterized by exponential sensitivity to initial conditions intrinsic to orbits on the attractor. The second exponent is zero (up to a calculation error) being associated with a perturbation of shift along the trajectory. The third exponent is negative and is responsible for the approach of the trajectories to the attractor. The fact that the sum of all the exponents is negative indicates the phase volume compression in the subspace (u, v, w). It is consistent with the analytical calculation of the divergence for the vector field determined by the right-hand sides of (4.1); namely, $\mathrm{div}\mathbf{F} = \partial_u f_u + \partial_v f_v + \partial_w f_w = -\mu_1 / A - \mu_2 / B - \mu_3 / Q$ (at the assumed parameters it equals –6).

5. Tanabe – Kaneko model

For a correct description of the plane problem of body motion in viscous fluid it is essential to account the dependence of the velocity circulation around the profile on the dynamical variables and parameters. For the body in the form of a thin flat plate the circulation can be evaluated on a base of the Kutta – Joukovsky – Chaplygin postulate of absence of singularity of the velocity field at the trailing edge of the profile moving in fluid [7-12]. Then, it becomes possible to evaluate using Joukovsky theorem the lift force and the drag force. Tanabe and Kaneko argue in their paper [23] that these effects may lead to arising complex dynamics and chaos in motion of the body falling in fluid due to gravity.

Using velocity components in the projection on the axis of the coordinate system associated with the body, one can simplify the equations suggested originally by Tanabe and Kaneko [23] and represent them as

$$\begin{aligned} &\dot{v}_x + k_{\|} v_x = \dot{\theta} v_y - g_0 \sin\theta + \pi\overline{\rho} v_y^2 \operatorname{sgn} v_x, \\ &\dot{v}_y + k_{\perp} v_y = -\dot{\theta} v_x - g_0 \cos\theta - \pi\overline{\rho} v_x v_y \operatorname{sgn} v_x, \\ &\ddot{\theta} + k_{\perp}\dot{\theta} = -3\pi\overline{\rho} l^{-1} v_x v_y, \end{aligned} \tag{5.1}$$

where $\overline{\rho} = \rho_f l / m$, $l = 2a$ is the width of the plate, g_0 is the gravity acceleration constant, m is the mass of the plate. The coefficients $k_{\|}$ and $k_{\perp}$ characterize the viscous friction for motion of the plate in fluid in the longitudinal and the transverse direction. To determine the coordinates of the center of mass in the laboratory frame, the system (5.1) is supplemented by equations

$$\dot{X} = v_x \cos\theta - v_y \sin\theta,\ \dot{Y} = v_x \sin\theta + v_y \cos\theta. \tag{5.2}$$

In the absence of friction, the equations (5.1) obviously correspond in structure to equations (1.6) if we set

$$\Gamma = -\pi l v_y \operatorname{sgn} v_x,\ A = B = 1,\ \frac{A-B}{a^2 Q} = -\frac{3\pi\overline{\rho}}{l},\ g(1-\rho) = g_0. \tag{5.3}$$

The fact that the second and the third equalities (5.3) contradict each other, is associated with some incorrectness of the Tanabe – Kaneko formulation of the problem that was criticized after publication of their work [24,25]. Namely, due to the fact that the authors excluded the added mass effect, the coefficients A and B appear to be equal, and it implies that the coefficient in the third equation (5.1) vanish, while in correct approach it should be relevant for the observed complex dynamics. Further, the formula for circulation Γ according to (5.3) takes into account only contribution of the translational motion of the plate, while there is also a contribution from the rotational motion proportional to the angular velocity [9, 28]. In addition, Tanabe and Kaneko excluded the Archimedean buoyancy.[2]

Despite these seemingly essential deficiencies, the Tanabe – Kaneko model qualitatively gives a reasonable picture of possible regimes of complex dynamics for the falling plate in fluid. This is confirmed by comparative analysis of this model with its corrected version and explained to some extent in Section 8.3.

We present here some numerical results for the model (5.1), taking the parameters chosen by the authors: $\overline{\rho} = 0.1$, $l = 1$, $g = 9.8$; the values $k_{\|}$ and $k_{\perp}$ will be varied.

To define the Poincaré map it is appropriate to determine cross-section of the flow of trajectories in four-dimensional phase space by a three-dimensional hyper-surface

$$S = \sin\theta = 0. \tag{5.4}$$

Calculation of the Poincaré map was implemented as a special sub-program that performs numerical integration of the differential equations by the Runge – Kutta fourth order method. To construct the Poincaré section in accordance with the condition (5.4), the method of Hénon was used [51, 15]. Specifically, numerical integration of the differential equations is continued up to detecting situation that at the next step the S value changes sign. Then, the last step is canceled, and an additional step is performed using the same difference method, but taking S as the independent variable, and with the step size given by the obtained value of S with the opposite sign. This returns the representative point on the surface S=0 and we get the Poincaré map image for the initial state vector. Note that the procedure is consistent in accuracy with the difference scheme used. A similar routine is performed at intersection of the phase trajectory with three-

[2] The last flaw, however, may be corrected readily by introducing a parameter of effective acceleration of free fall, $g_0 = g(1-\rho)$, and in some cases, like fall of the plate in the air, it is naturally insignificant.

dimensional hypersurface u=0 to avoid loss of accuracy of the difference scheme by accurate localization of the passage in time.

To draw charts of dynamic regimes a procedure of scan of the parameter plane of $k_\perp$ and $f = k_\perp / k_\parallel$ is carried out on a grid with some steps along two coordinate axes. At each point about 10^3 iterations of the Poincaré map are produced, and the data for the final iteration steps are analyzed to detect a repetition period (from 1 to 14) up to some level of permissible error. If a certain period is detected, the pixel in the diagram is attributed with the corresponding color, and the routine proceeds with analysis of the next point in the parameter plane. To start iterations at each new point it is reasonable to use a state obtained as result of iterations at the previous point ("scan with inheritance"). In most cases it helps to speed up essentially the convergence to sustained dynamics.

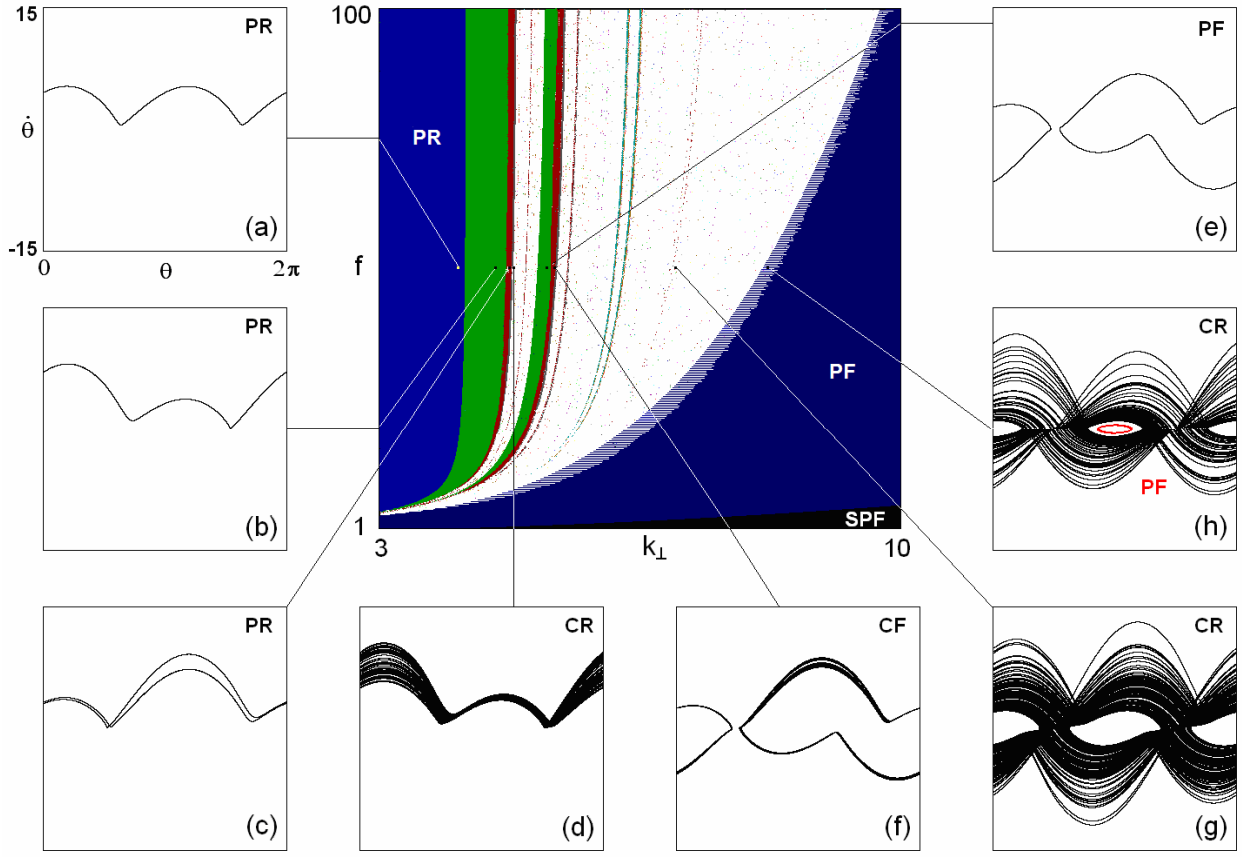

Figure 11: Chart of dynamical regimes in the parameter plane $k_\perp$, $f = k_\perp / k_\parallel$ for the Tanabe – Kaneko model. Values of other parameters are $\overline{\rho} = 0.1$, $l = 1$, $g = 9.8$. The color is determined from analysis of the repetition period in the Poincaré section (blue designates period 1 with symmetry, and green – without symmetry, other colors correspond to larger periods). The white color means chaos or unrecognized regular regimes. Black color designates stationary fall (SPF). On the periphery portraits of attractors are shown for regimes corresponding to the Tanabe – Kaneko classification scheme: PR (periodic rotation), CR (chaotic rotation), RF (periodic flutter, oscillations without tumbling), CF (chaotic flutter). Blue and white horizontal shading corresponds to coexistence of attractors associated with chaotic rotation and periodic oscillations, as illustrated by the diagram (h).

Figure 11 shows a chart of dynamical regimes. On the periphery portraits of attractors are collected corresponding to some representative points on the parameter plane. Visually, the phase portraits in the plane $(\theta, \dot{\theta})$ allow easy drawing conclusions about nature of the regimes of the fall. If the orbit or a set of orbits belonging to the attractor goes around the phase cylinder, the regime is classified as autorotation that may be periodic (PR, diagrams (a), (b), (c)) or chaotic (CR, diagrams (d), (g), (h)). If no orbits around the phase cylinder occur, this corresponds to a fall with oscillations without tumbling that is flutter, which may be periodic (PF, diagram (e)), or

chaotic (CF, diagram (f)). The black area at the bottom left of the chart corresponds to the steady perpendicular fall without oscillations (SPF).

Full spectrum of Lyapunov exponents of the system (5.1), (5.2) includes two zero ones corresponding to shift perturbations for coordinates X and Y of the center of mass, and four exponents relating to the attractor of the subsystem (5.1). One of them is zero as associated with a shift along the reference phase trajectory on the attractor.

Because of presence of a discontinuous sgn-function in (5.1), it is preferable to compute Lyapunov exponents without appealing to the linearized equations in variations [15]. Namely, at given parameters, using the subroutine computing the Poincaré map, we perform iterations jointly for a collection of four states, one of which corresponds to the reference trajectory, and three others to slightly perturbed orbits close to the reference one. After each step, the perturbation vectors are orthogonalized by the Gram – Schmidt procedure and normalized to a fixed small norm, and the computation continues with the redefined perturbation vectors. Three non-trivial Lyapunov exponents are evaluated as coefficients of the growth or decay of the accumulated sums of the logarithm of the perturbation magnitude ratios.

In systems with symmetry, as known, a symmetric limit cycle can not undergo the period doubling; a bifurcation of symmetry breaking must preceded [52].

Increasing the value of $k_\perp$, i.e. moving on the chart of Fig.11 along a horizontal path from left to right, one observes the symmetry breaking corresponding to transition from blue to green area and then it is followed by a cascade of period-doubling bifurcations and onset of chaos.

Figure 12 shows a one-parameter bifurcation diagram ("bifurcation tree") and the parameter dependence of the senior non-trivial Lyapunov exponent illustrating the period doubling transition to chaos. Diagrams correspond to the horizontal path on the chart at f=50 varying $k_\perp$ in certain limits. The diagrams demonstrate a well-recognizable typical visual image of transition to chaos through an infinite cascade of period-doubling bifurcations manifesting universality and scaling of Feigenbaum [54, 55, 14, 15]. This qualitative conclusion is confirmed by the numerical estimates for the constant of convergence of bifurcation points ($\delta \approx 4.67$) and the constant characterizing the splitting of the branches of the "tree" ($\alpha \approx -2.50$).

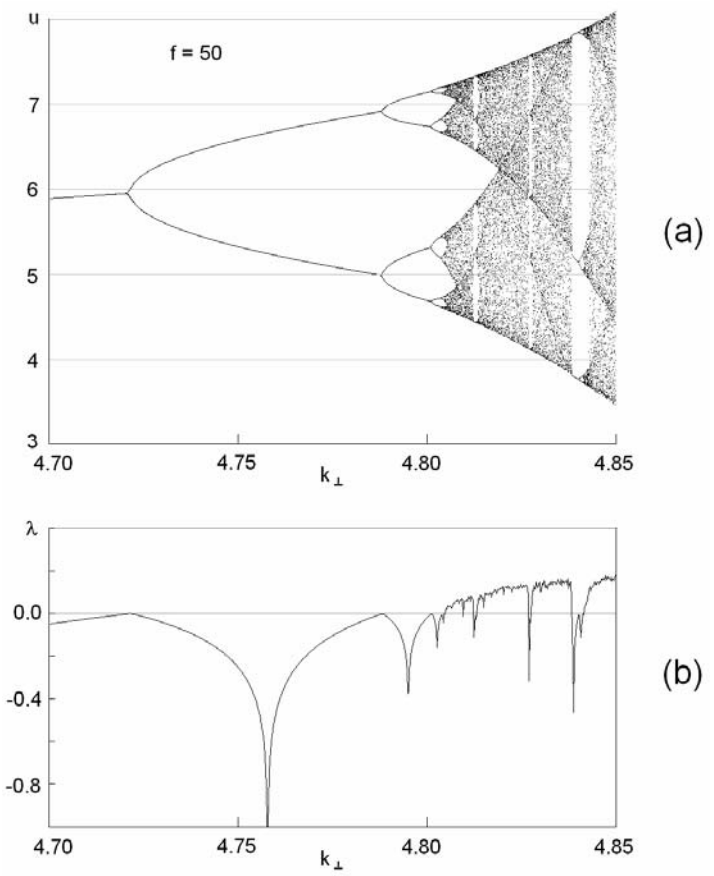

Figure 12. Bifurcation tree and the largest nontrivial Lyapunov exponent parameter dependence illustrating transition to chaos through period-doubling bifurcations in the Tanabe – Kaneko model along the horizontal path f=50 on the chart of regimes of Figure 11.

Figure 13 reproduces portraits of attractors for Tanabe – Kaneko model similar to those in their original paper. Along the coordinate axes the components of translational velocity in the laboratory frame determined according to (5.2) are plotted. The Lyapunov exponents of these attractors (except zero ones, related to the subsystem (5.2)) obtained in the computations are given in the figure caption. Attractor in the diagram (a) is regular and consists of a single closed orbit that is a limit cycle, so that the senior exponent is zero, and the others are negative. Attractors (b) and (c) are characterized by the presence of a positive exponent that indicates the chaotic nature of the regime. The sum of the exponents in each case is negative that means compression of the phase volume in the subspace $(u, v, \theta, \dot{\theta})$ in the course of time evolution. Its value is consistent with analytical calculation of the divergence of the vector field whose components are given by the right side of (5.1) : $\mathrm{div}\mathbf{F} = -k_{\|} - 2k_{\perp}$.

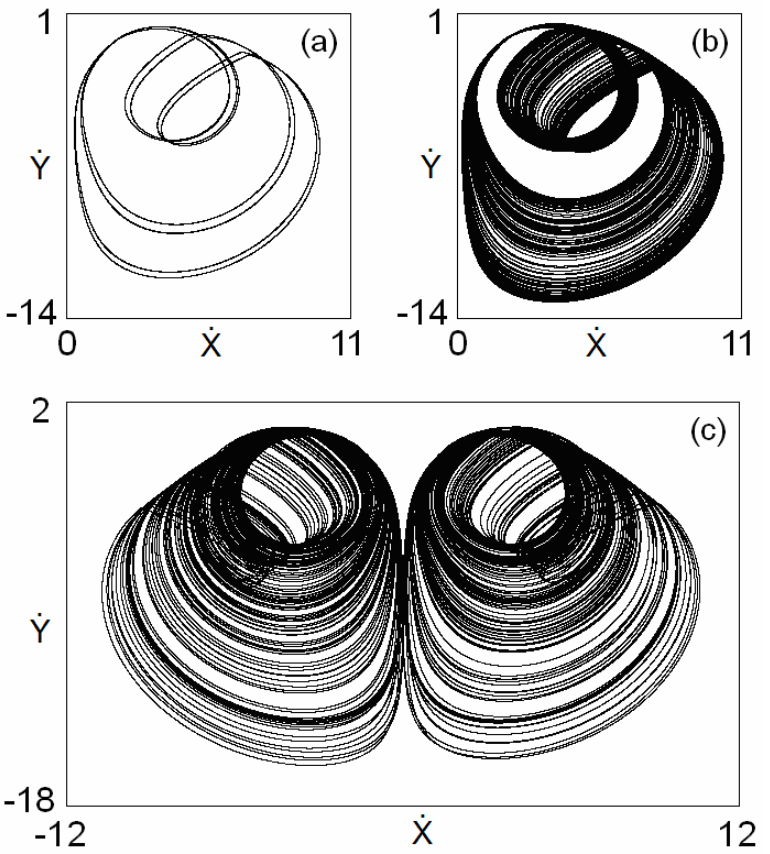

Figure 13: Phase portraits of attractors for the Tanabe – Kaneko model at $k_\perp$=4.84 (a), 4.9 (b), 5 (c). Other parameters: $\overline{\rho}=0.1$, $l=1$, $g=9.8$, $k_\parallel$=100$k_\perp$. Along the coordinate axes components of translational velocity in the laboratory frame $\dot{X}=v_x\cos\theta-v_y\sin\theta$, $\dot{Y}=v_x\sin\theta+v_y\cos\theta$ are plotted. Lyapunov exponents are: a) $\{0,-0.085,-2.026,-7.62\}$, b) $\{0.162\pm0.005,\ 0,\ -2.23\pm0.01,-7.78\pm0.1\}$, c) $\{0.345\pm0.007,\ 0,\ -2.36\pm0.01,-7.86\pm0.05\}$.

Let us discuss in some detail the transition from a steady fall to oscillations (flutter) in the Tanabe – Kaneko model. A non-standard nature of the bifurcation occurs due to the fact that the equations contain a discontinuous function sgn.

Considering solutions close to the of steady fall regime: $\theta=0, v_x=0$, $v_y=-g_0/k_\perp$, we put $\theta=\vartheta, v_x=u, v_y=-g_0k_\perp^{-1}+v$, where $|\vartheta|<<1, |u|<<1$, $|v|<<1$. If we ignore perturbations of the transverse velocity v_y (with relatively large factor $k_\perp$ it seems reasonable), the equations for the other variables read

$$\begin{aligned}\dot{u}+k_\parallel u+g_0\xi&=\pi\overline{\rho}g_0^2k_\perp^{-2}\operatorname{sgn}u,\\ \dot{\xi}&=3\pi\overline{\rho}g_0l^{-1}k_\perp^{-2}u,\end{aligned}\qquad(5.5)$$

where $\xi=k_\perp^{-1}\dot{\vartheta}+\vartheta$. Hence, for ξ we obtain an equation of the same form as that for an oscillator with dry friction [53]

$$\ddot{\xi}+k_\parallel\dot{\xi}+\omega^2\xi=F\operatorname{sgn}\dot{\xi},\qquad(5.6)$$

with $\omega^2=3\pi\overline{\rho}g_0^2l^{-1}k_\perp^{-2}$, $F=3\pi^2\overline{\rho}^2g_0^3l^{-1}k_\perp^{-4}$. However, the factor responsible for the "dry friction" has a sign opposite to that in the standard problem.

First, let us assume for simplicity that $k_\parallel=0$. In the upper half-plane $(\xi,\dot{\xi})$ the family of phase trajectories is represented by ellipses centered on the x-axis at $\xi=F\omega^{-2}=\pi\overline{\rho}gk_\perp^{-2}$ (point A in Fig. 14a), and in the lower half-plane by ellipses centered at $\xi=-F\omega^{-2}$ (point B in Fig. 14a).

Since $F > 0$, the motion is accompanied by the growing oscillations (the amplitude increases linearly in time).

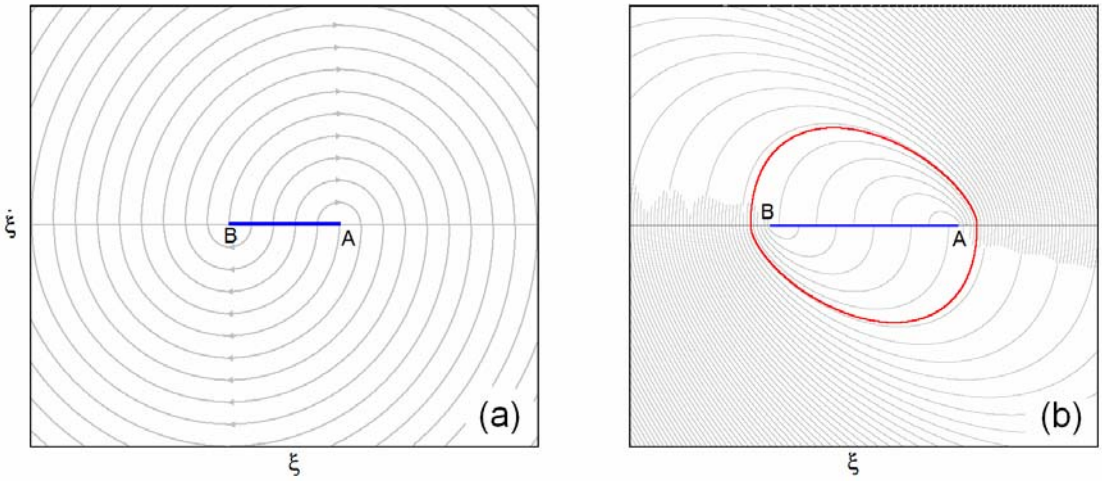

Figure 14: Phase trajectories for equations (5.6) on the plane $(\xi,\dot{\xi})$ in the case $k_{\|}=0$ (a) and $0<k_{\|}<k_*$ (b). The horizontal segment AB consists of unstable fixed points. Red in the diagram (b) designates the stable limit cycle.

Suppose now that the coefficient $k_{\|}$ is positive. While it is not large, in the upper half-plane instead of ellipses we have a family of trajectories spiraling to point A, and in the lower half-plane to the point B. The corresponding oscillation frequency and damping coefficient are determined by the imaginary and real parts of the roots of the characteristic equation $\lambda^2+k_{\|}\lambda+\omega^2=0$: $\lambda_{1,2}=k_{\|}/2\pm i\sqrt{\omega^2-k_{\|}^2/4}$. In contrast to the previous case, the oscillating motion visiting the upper and lower half-planes turn by turn converges to a limit cycle encompassing the segment AB. The situation will change when the character of the decay becomes not oscillating but monotonous, that is the case $k_{\|}^2>4\omega^2$. Returning to parameters of the Tanabe – Kaneko model, we see that it corresponds to the condition

$$f=\frac{k_\perp}{k_{\|}}<\left(\frac{k_\perp}{k_*}\right)^2,\quad k_*=\sqrt[4]{12\frac{\pi\bar{\rho}g_0^2}{l}}$$

On the chart of regimes the corresponding area is shown in black. Numerical simulations show that in this area the steady fall occurs, while outside it the oscillations develop (flutter).[3]

6. Belmonte – Eisenberg – Moses model

Starting from some experiments with plates falling in fluid the authors [27] turn to formulation of the problem, in which the resistance forces for the translational and rotational motions depend on the velocities quadratically:

$$F_x=-\tfrac{1}{4}\alpha_{\|}\rho_f lV v_x,\ F_y=-\tfrac{1}{4}\alpha_\perp\rho_f lV v_y,\ F_\theta=-\tfrac{1}{4}\alpha_\omega\rho_f l^4|\dot{\theta}|\dot{\theta},\qquad(6.1)$$

where $V=\sqrt{v_x^2+v_y^2}$, $\alpha_{\|}$, $\alpha_\perp$, and α_ω are constant coefficients. Equations analogous to those of Tanabe – Kaneko in this case take the form

[3] The simplified equation (5.1) can be considered as a reasonable approximation until $\vartheta<1$. Since $|\vartheta|\sim|\xi_{A,B}|$ this implies $|\xi_{A,B}|<1$. With $\bar{\rho}=0.1$, $l=1$, and $g=9.8$ we have $k_*=4.36$ and $\pm\xi_{A,B}=\pi\bar{\rho}gk_\perp^{-2}\approx 3k_\perp^{-2}$, so the condition $3k_\perp^{-2}<1$ must be valid. The black area in the chart of regimes is placed in that part of the parameter plane where this condition is well satisfied.

$$\begin{aligned}
\dot{v}_x &= -\tfrac{1}{4}\alpha_{\|}\bar{\rho}Vv_x - g^*\sin\theta + \pi\bar{\rho}v_y^2\operatorname{sgn}v_x + \dot{\theta}v_y,\ V=\sqrt{v_x^2+v_y^2}\\
\dot{v}_y &= -\tfrac{1}{4}\alpha_{\perp}\bar{\rho}Vv_y - g^*\cos\theta - \pi\bar{\rho}v_xv_y\operatorname{sgn}v_x - \dot{\theta}v_x,\\
\ddot{\theta} &= -3\alpha_{\omega}\bar{\rho}l\,|\dot{\theta}|\,\dot{\theta} + 3l^{-1}\pi\bar{\rho}v_xv_y,
\end{aligned} \tag{6.2}$$

where the same notation is used as in (5.1), and the constant g^* characterizes the acceleration of gravity reduced with account of the Archimedean buoyancy.

The authors emphasize the fact that due to the quadratic dependence of the resistance forces the above equations rewritten in a dimensionless form contain a well-known in hydrodynamics characteristic parameter, the Froude number Fr. Namely, the change of variables and parameters

$$v_x = 2v_x'\sqrt{\frac{g^*}{\bar{\rho}}},\ v_y = 2v_y'\sqrt{\frac{g^*}{\bar{\rho}}},\ t = t'\sqrt{\frac{l}{g^*}},\ \mathrm{Fr} = \frac{2}{\sqrt{\bar{\rho}l}}, \tag{6.3}$$

reduces the equations (6.2) to

$$\begin{aligned}
\dot{v}_x &= (-\alpha_{\|}Vv_x - \sin\theta + 4\pi v_y^2\operatorname{sgn}v_x)/\mathrm{Fr} + \dot{\theta}v_y,\ V=\sqrt{v_x^2+v_y^2}\\
\dot{v}_y &= (-\alpha_{\perp}Vv_y - \cos\theta - 4\pi v_xv_y\operatorname{sgn}v_x)/\mathrm{Fr} - \dot{\theta}v_x,\\
\ddot{\theta} &= -12\cdot\alpha_{\omega}\,|\dot{\theta}|\,\dot{\theta}/\mathrm{Fr}^2 + 12\pi v_xv_y,
\end{aligned} \tag{6.4}$$

where the primes are omitted for brevity. The authors take the values of the coefficients

$$\alpha_{\|} = 0.88,\ \alpha_{\perp} = 4.1,\ \alpha_{\omega} = 0.0674\,. \tag{6.5}$$

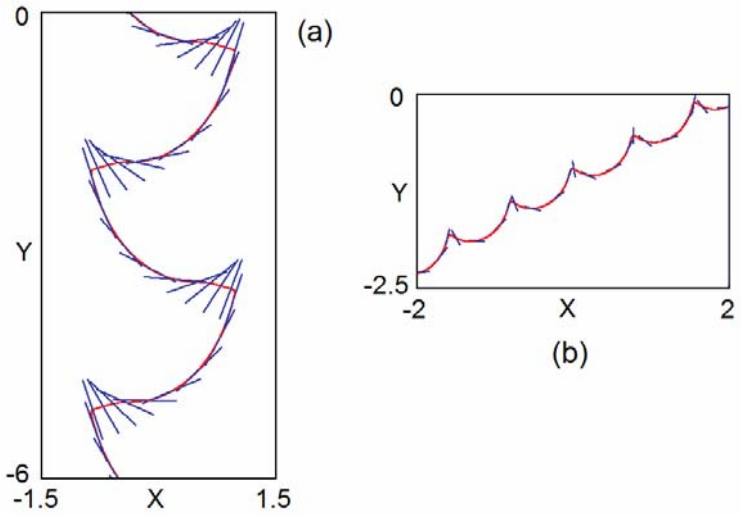

Figure 15. Illustrations of motion of the plate in fluid: self-oscillation mode at Fr=0.45 (a) and autorotation at Fr=0.89 (b) according to results of numerical simulation with equations (6.4)

Figure 15 shows the diagrams obtained by numerical integration of (6.4), which reproduce the results of [27]. The illustrations (a) and (b) correspond to the fall with oscillations (flutter) and tumbling (autorotation), respectively. Fig. 16 shows portraits of attractors corresponding to these motions in projections on the planes (v_x, v_y) and $(\theta, \dot{\theta})$. From the diagrams in the right column one can see that in one case the observed motion corresponds to the limit cycle of the first kind, and in the other one to the limit cycle of the second kind (going around the phase cylinder).

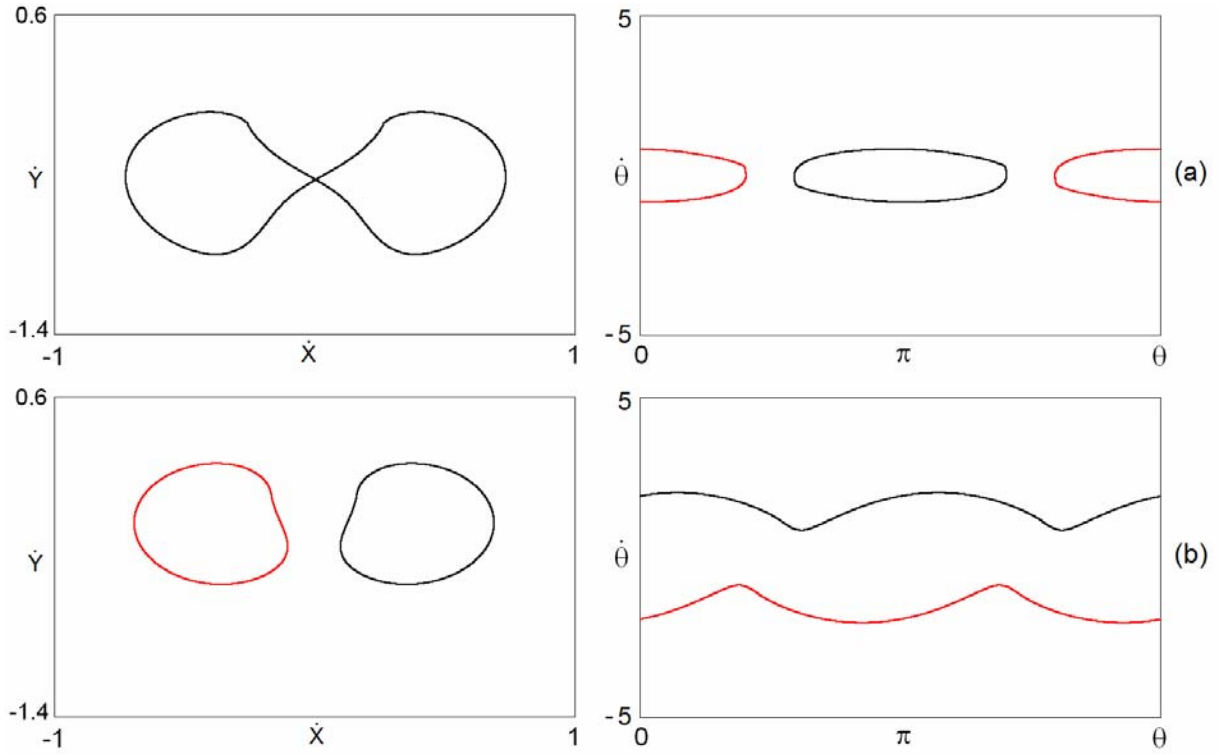

Figure 16: Phase portraits of attractors corresponding to flutter at Fr=0.45 (a) and to autorotation at Fr=0.89 (b) according to the results of the numerical solution of equations (6.1). Black and red colors show the coexisting attractors.

The model (6.2), like the original Tanabe – Kaneko model, does not take into account the added masses and moment of inertia, as well as a correction to the circulation due to the rotational motion. So it makes sense to consider a modification of the equations in the same style as in the corrected Tanabe – Kaneko model (see Section 8).

7. Andersen – Pesavento – Wang model

Among systems discussed in this review, the work of Andersen, Pesavento and Wang [28] is the most elaborated attempt to describe the fall of a flat plate or a body with elliptic profile in fluid by means of a finite-dimensional model. The authors start with equations (1.2) and add there the terms accounting resistance of the medium to the translational motion, F_x, F_y and the torque of the friction force F_θ:

$$\begin{aligned}
(m+m_x)\dot v_x &= (m+m_y)v_y\dot\theta - \rho_f\Gamma v_y - mg(1-\rho_f\rho_s^{-1})\sin\theta - F_x,\\
(m+m_y)\dot v_y &= -(m+m_x)u\dot\theta + \rho_f\Gamma v_x - mg(1-\rho_f\rho_s^{-1})\cos\theta - F_y,\\
(I+J)\ddot\theta &= (m_x-m_y)v_xv_y - F_\theta.
\end{aligned} \qquad (7.1)$$

Basing on numerical simulations with Navier – Stokes equations for the two-dimensional hydrodynamic flow around elliptic profiles [28, 30], the authors propose the following approximate expressions for the circulation and the resistance forces:

$$\begin{aligned}
\Gamma &= -2C_T a\frac{v_xv_y}{\sqrt{v_x^2+v_y^2}} + 2C_Ra^2\dot\theta,\\
\begin{pmatrix}F_x\\F_y\end{pmatrix} &= \rho_f a\left(C_A - C_B\frac{u^2-v^2}{v_x^2+v_y^2}\right)\sqrt{v_x^2+v_y^2}\begin{pmatrix}v_x\\v_y\end{pmatrix},\\
F_\theta &= \pi\rho_f a^4\left(\mu_1+\mu_2|\dot\theta|\right)\dot\theta.
\end{aligned} \qquad (7.2)$$

In calculations, the following numerical values of the coefficients are adopted:

$$C_T = \tfrac{6}{5},\ C_R = \pi,\ C_A = \tfrac{7}{5},\ C_B = 1, \tag{7.3}$$

while μ_1 and μ_2 are supposed to be varied.

Let us substitute the expressions (1.4), (1.5) for the mass, the moment of inertia, the added masses, and the added moment of inertia in equation (7.1) and introduce the notation

$$I^* = \frac{b\rho_s}{a\rho_f},\ \beta = \frac{b}{a}. \tag{7.4}$$

Normalizing velocity components and time to get the unit coefficients at the terms responsible for the gravity,

$$u = \frac{v_x}{a\sqrt{gI^*(1-\rho)}},\ v = \frac{v_y}{a\sqrt{gI^*(1-\rho)}},\ t' = t\sqrt{gI^*(1-\rho)}\,. \tag{7.5}$$

we obtain

$$\begin{aligned}
&(I^* + \beta^2)\dot{u} = (I^* + 1)v\dot{\theta} - \overline{\Gamma}v - \sin\theta - Ku,\\
&(I^* + 1)\dot{v} = -(I^* + \beta^2)u\dot{\theta} + \overline{\Gamma}u - \cos\theta - Kv,\\
&(\tfrac{1}{4}(1+\beta^2)I^* + \tfrac{1}{8}(1-\beta^2)^2)\ddot{\theta} = (\beta^2 - 1)uv - K_\theta\dot{\theta}.
\end{aligned} \tag{7.6}$$

In the limit $\beta \to 0$ corresponding to the thin flat plate, the equations reduce to

$$\begin{aligned}
&I^*\dot{u} = (I^* + 1)v\dot{\theta} - \overline{\Gamma}v - \sin\theta - Ku,\\
&(I^* + 1)\dot{v} = -I^*u\dot{\theta} + \overline{\Gamma}u - \cos\theta - Kv,\\
&(\tfrac{1}{4}I^* + \tfrac{1}{8})\ddot{\theta} = -uv - K_\theta\dot{\theta}.
\end{aligned} \tag{7.7}$$

In accordance with (7.2), in (7.6) and (7.7) we set

$$\begin{aligned}
&\overline{\Gamma} = \frac{2}{\pi}\left(-C_T\frac{uv}{\sqrt{u^2+v^2}} + C_R\dot{\theta}\right),\ K = \frac{1}{\pi}\left(C_A - C_B\frac{u^2-v^2}{u^2+v^2}\right)\sqrt{u^2+v^2},\\
&K_\theta = \mu_1' + \mu_2|\dot{\theta}|,\ \ \mu_1' = \mu_1\sqrt{gI^*(1-\rho)}.
\end{aligned} \tag{7.8}$$

To compute the dimensionless coordinates for the center of mass of the falling body, together with (7.6) or (7.7) the equations have to be solved

$$\dot{X} = u\cos\theta - v\sin\theta,\ \ \dot{Y} = u\sin\theta + v\cos\theta. \tag{7.9}$$

In Ref. [28] Anderson, Pesavento and Wang, not emphasizing this point specially, limit themselves with a special case introducing coefficients, which satisfy, accidentally or not, the relation $C_T = \frac{1}{2}(C_A + C_B)$. Due to this, some terms in the equations disappear, and derivation of stability loss condition for the uniform steady fall simplifies substantially. The equations reduce to the form

$$\begin{aligned}
&I^*\dot{u} = (I^* - 1)v\dot{\theta} - \frac{2u^3}{5\pi\sqrt{u^2+v^2}} - \sin\theta,\\
&(I^* + 1)\dot{v} = (2 - I^*)u\dot{\theta} - \frac{14u^2 + 12v^2}{5\pi\sqrt{u^2+v^2}}v - \cos\theta,\\
&(\tfrac{1}{4}I^* + \tfrac{1}{8})\ddot{\theta} = -uv - \left(\mu_1' + \mu_2|\dot{\theta}|\right)\dot{\theta}
\end{aligned} \tag{7.10}$$

and their linearization nearby the fixed point $u = 0,\ v = -V = -\sqrt{5\pi/12}$, $\theta = 0,\ \dot{\theta} = 0$ yields

$$I^*\dot{\tilde{u}} = -(I^* - 1)V\tilde{\theta} - \tilde{\theta},\ \ (\tfrac{1}{4}I^* + \tfrac{1}{8})\ddot{\theta} = Vu - \mu_1'\dot{\tilde{\theta}}. \qquad (7.11)$$

The exponential substitution $\tilde{u}, \tilde{\theta} \sim e^{st}$ leads to the characteristic equation

$$s^3(\tfrac{1}{4}I^* + \tfrac{1}{8})I^* + s^2\mu_1'I^* + s(I^* - 1)V^2 + V = 0. \qquad (7.12)$$

Condition of stability loss, which consists in vanishing the real part for a pair of complex conjugate roots, can be found, if we search for solution as $s = i\zeta$ where ζ is real. Then

$$\zeta^3(\tfrac{1}{4}I^* + \tfrac{1}{8})I^* = (I^* - 1)V^2\zeta,\ \ \zeta^2\mu_1'I^* = V, \qquad (7.13)$$

and the critical value of the coefficient of friction is evaluated as [28]

$$\mu_* = \frac{2I^* + 1}{8V(I^* - 1)} = \frac{1}{4}\sqrt{\frac{3}{5\pi}}\,\frac{2I^* + 1}{I^* - 1}. \qquad (7.14)$$

Stability loss of the fixed point corresponds to a supercritical (normal) Andronov – Hopf bifurcation [44, 45, 19], which results in appearance of the limit cycle associated with periodic self-oscillations of the plate from side to side (the flutter) in the region $\mu_1' < \mu_*$. Note that such bifurcation occurs only with taking into account the viscous resistance to the body rotation. If the resistance torque is quadratic in the angular velocity, i.e. μ_1=0, then near the state of steady uniform fall the linear dynamics is conservative, and a correct stability analysis should take nonlinear terms into account.

Fig. 17 shows a chart of regimes of the model (7.10) in the plane of parameters I^* and μ, drawn under a condition $\mu_1' = \mu_2 = \mu$ that corresponds to a two-dimensional phase diagram in the original paper of Anderson, Pesavento, and Wang [28]. The chart is obtained by the method described above for the Tanabe – Kaneko model; scanning is performed in the upward direction with inheritance. Colored areas on the chart indicate periodicity in the numerical iterations of the Poincaré map counting passages of zeros of the function $\sin\theta$. A method for computation of the Poincaré map is analogous to that for the Tanabe – Kaneko model, but simpler because now the equations do not contain discontinuous coefficients.

The dotted line on the chart indicates threshold of stability loss for the fixed point (7.14). Crossing this border from black to dark blue domain is accompanied by appearance of self-oscillations (flutter, the domain PF). Domain PR corresponds to the periodic autorotation. Blue indicates regimes where the system manifests a single-turn limit cycle with symmetry, and green without symmetry. Other colors relate to larger periods. White areas correspond to chaos or unrecognized regular motions.

Fig. 18 shows phase portraits of attractors for the model (7.10) at several representative points of the parameter plane (see the figure caption). The portraits are drawn on the plane of dimensionless velocity components in the laboratory frame, to make possible visual comparison with analogous pictures for the Tanabe – Kaneko model in Fig. 13. Coexisting attractors can be seen in diagrams (c) – (e) shown in black and red.

Lyapunov exponents of the attractors have been computed and are given in the figure caption. (Beside them, there are two zero exponents in each case, relating to the subsystem (7.9)). In the cases (e) and (f) chaotic attractors occur possessing a positive Lyapunov exponent. The second exponent is the zero, while the others are negative. In the cases (a) – (d) attractors are limit cycles, in which the senior exponent is zero, and the others are negative. The sum of all the exponents in each case is negative indicating compression of the phase volume in the course of approach of phase trajectories to the attractor.

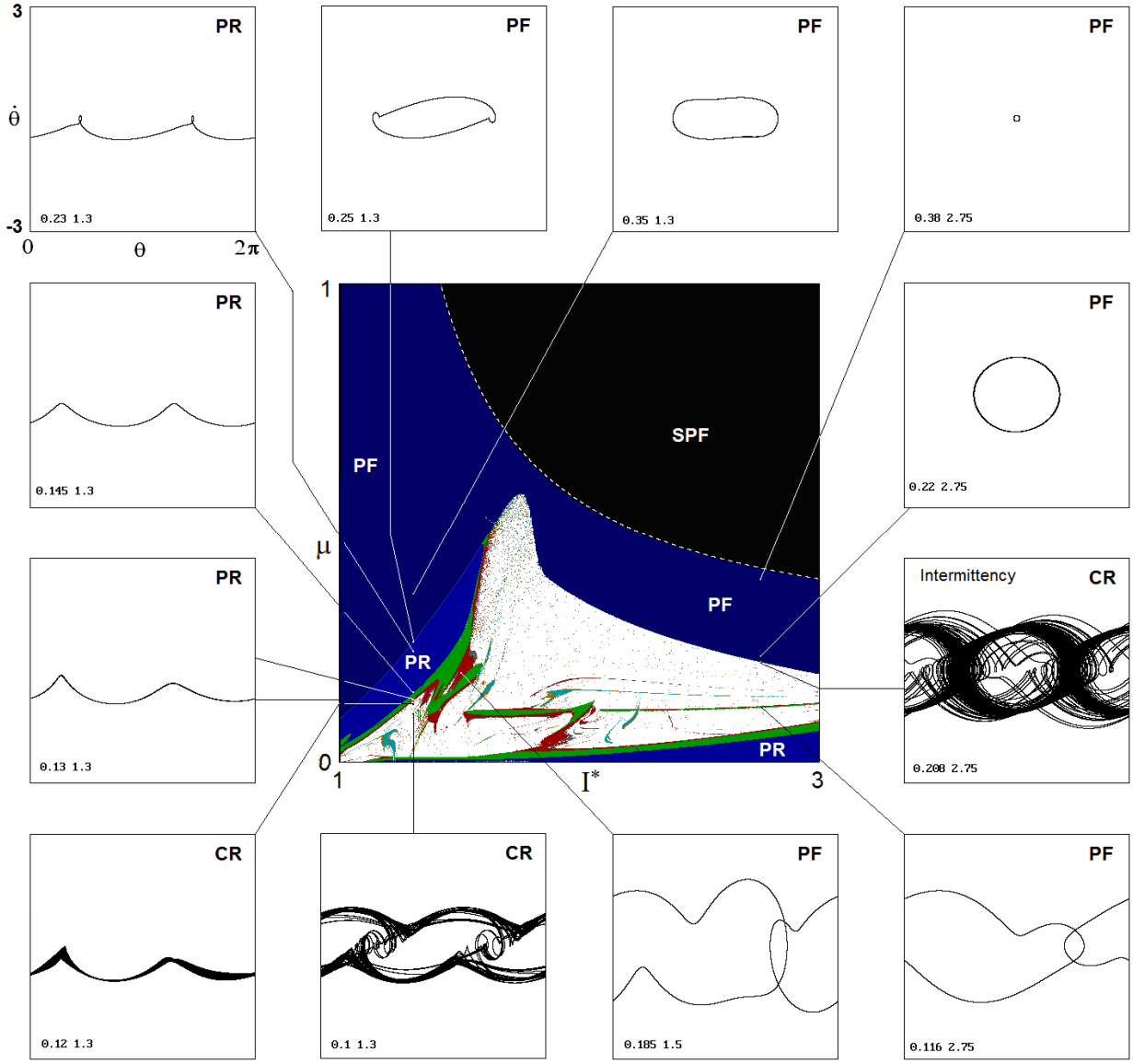

Figure 17: Chart of regimes in the plane of parameters I^* and μ for the model (7.10), where $\mu_1 = \mu_2 = \mu$. On the periphery portraits of attractors are shown illustrating periodic rotation PR, chaotic rotation CR, periodic flutter PF, chaotic flutter CF. Colors indicate periods observed in iteration of the Poincaré map as obtained by scanning the plane upward with inheritance. Blue indicates the period 1 regimes with symmetry, and green the period 1 regimes without symmetry, other colors correspond to larger periods. White areas correspond to chaos or unrecognized motions. Black designates a simple perpendicular fall (SPF). The dotted line indicates the stability loss threshold for the fixed point (7.14).

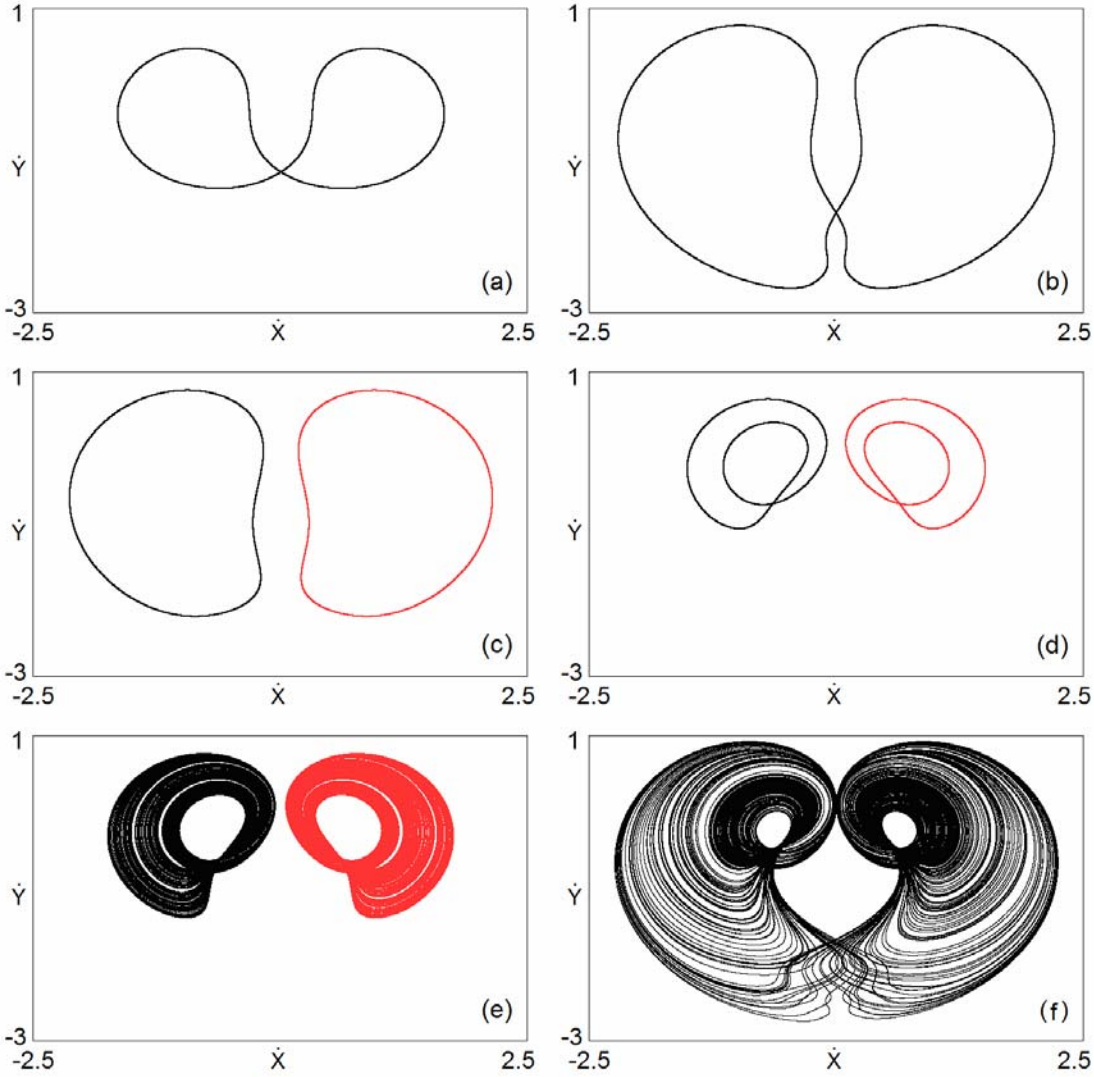

Figure 18: Phase portraits of attractors for Andersen – Pesavento – Wang model (7.10) at $\mu_{1,2}$=0.35 (a), 0.25 (b), 0.23 (c), 0.13 (d), 0.12 (e), 0.1 (f). Other parameters: I^*=1.3, C_T=1.2, C_R=π, C_A=1.4, C_B=1.0. Coexisting attractors are shown in black and red. Lyapunov exponents for these attractors: {0, −0.135, −0.91, −1.075} (a), {0, −0.0159, −0.871, −0.934} (b), {0, −0.158, −0.792, −0.827} (c), {0, −0.0353, −0.362, −0.766} (d), {0.051, 0, −0.435, −0.735} (e), {0.073, 0, −0.474, −0.690} (f).

8. Generalized model

For the discussed finite-dimension models of body falling in fluid it would be interesting to provide mutual comparison of their dynamics, but it is complicated by the fact that all the authors use different normalizations of the equations. Below we reformulate the equations in such way that they cover all these models using common dimensionless variables and parameters. We outline specially the limit case of the profile degenerating to the thin plate. We prefer the normalization which was used in Section 3 for the equations of Kozlov model in version (3.16). For the model of Tanabe – Kaneko, which was criticized for some hydrodynamic incorrectness [24, 25], and, analogously, for the Belmonte – Eisenberg – Moses model, we will consider improved versions taking into account those critical remarks.

8.1. Equations and normalization

As initial form of the equations let us take that of Anderson, Pesavento and Wang (7.1), which relates to the body of elliptical profile with semi-axes a and b falling in fluid in the presence of circulation Γ and resistance forces, characterized by coefficients $K_{x,y,\theta}$. Assuming

$$\Gamma = \pi a^2 \overline{\Gamma}\,, \tag{8.1}$$

$$F_x = \pi\rho_f a^3 K_x u,\ F_y = \pi\rho_f a^3 K_y v,\ F_\theta = \pi\rho_f a^4 K_\theta \dot{\theta}, \tag{8.2}$$

and substituting the masses and moments of inertia for the elliptical profile (1.4), (1.5) with notation $\rho = \rho_f \rho_s^{-1}$ $\beta = b/a$, $u = v_x / a$, $v = v_y / a$ we obtain from (7.1) the set of equations

$$\begin{aligned}
&(1+\rho\beta)\dot{u} = (1+\rho\beta^{-1})v\dot{\theta} - \rho\beta^{-1}\overline{\Gamma}v - ga^{-1}(1-\rho)\sin\theta - \rho\beta^{-1}K_x u,\\
&(1+\rho\beta^{-1})\dot{v} = -(1+\rho\beta)u\dot{\theta} + \rho\beta^{-1}\overline{\Gamma}u - ga^{-1}(1-\rho)\cos\theta - \rho\beta^{-1}K_y v,\\
&(\tfrac{1}{4}(1+\beta^2) + \tfrac{1}{8}\rho\beta^{-1}(1-\beta^2)^2)\ddot{\theta} = \rho(\beta-\beta^{-1})uv - \rho\beta^{-1}K_\theta\dot{\theta}.
\end{aligned} \tag{8.3}$$

In the limit corresponding to a thin plate $\beta \to 0$, $\rho \to 0$, $r = \rho\beta^{-1}$ that gives

$$\begin{aligned}
&\dot{u} = (1+r)v\dot{\theta} - r\overline{\Gamma}v - ga^{-1}\sin\theta - rK_x u,\\
&(1+r)\dot{v} = -u\dot{\theta} + r\overline{\Gamma}u - ga^{-1}\cos\theta - rK_y v,\\
&(\tfrac{1}{4}+\tfrac{1}{8}r)\ddot{\theta} = -ruv - rK_\theta\dot{\theta}.
\end{aligned} \tag{8.4}$$

As a final step, we use normalization of time and velocity components

$$u = u'\sqrt{ga^{-1}},\ v = v'\sqrt{ga^{-1}},\ t = t'\sqrt{g^{-1}a} \tag{8.5}$$

and, omitting the primes for brevity, arrive at the equations

$$\begin{aligned}
&\dot{u} = (1+r)v\dot{\theta} - r\overline{\Gamma}v - \sin\theta - rK_x u,\\
&(1+r)\dot{v} = -u\dot{\theta} + r\overline{\Gamma}u - \cos\theta - rK_y v,\\
&(\tfrac{1}{4}+\tfrac{1}{8}r)\ddot{\theta} = -ruv - rK_\theta\dot{\theta}.
\end{aligned} \tag{8.6}$$

Dimensionless coordinates for the center of mass of the falling plate are determined by equations

$$\dot{X} = u\cos\theta - v\sin\theta,\ \dot{Y} = u\sin\theta + v\cos\theta. \tag{8.7}$$

With zero circulation $\overline{\Gamma} = 0$ and constant coefficients of the resistance forces

$$K_{x,y,\theta} = k_{1,2,3}, \tag{8.8}$$

from (8.6) we get **the Kozlov model** (3.16).

Next, let us introduce the circulation determined by the motion of the plate in fluid on the basis of the Kutta – Joukovsky – Chaplygin postulate. It may be done using the formula from the book of Sedov [9], which takes into account both contributions from translational and rotational components of the motion: $\Gamma = -2\pi a v_y \operatorname{sgn} v_x + \pi\dot{\theta}a^2$, or, in the normalization adopted here,

$$\overline{\Gamma} = -2v\operatorname{sgn} u + \dot{\theta}. \tag{8.9}$$

Then, with the drag coefficients (8.8) we obtain from (8.6) a set of equations corresponding to **the modified Tanabe – Kaneko model**.

Postulating the same relation for the circulation (8.9) and setting

$$\begin{aligned}
&K_x = \alpha'_{\parallel}\sqrt{u^2+v^2},\ K_y = \alpha'_{\perp}\sqrt{u^2+v^2},\ K_\theta = \alpha'_\omega\,|\,\dot{\theta}\,|,\\
&\alpha'_{\parallel} = \alpha_{\parallel}/2\pi = 0.14,\ \alpha'_{\perp} = \alpha_{\perp}/2\pi = 0.65,\ \alpha'_\omega = 4\alpha_\omega/\pi = 0.086,
\end{aligned} \tag{8.10}$$

we arrive at **the modified Belmonte – Eisenberg – Moses model.**

Finally, the equations of **the Anderson – Pesavento – Wang model** in the new normalization are obtained from (8.6) by substitutions

$$\overline{\Gamma} = \frac{2}{\pi}\left(-C_T \frac{uv}{\sqrt{u^2+v^2}} + C_R\dot{\theta} \right),\ C_T = 1.2,\ C_R = \pi,$$

$$K_x = K_y = \frac{1}{\pi}\left(C_A - C_B \frac{u^2-v^2}{u^2+v^2} \right)\sqrt{u^2+v^2},\ C_A = 1.4,\ C_B = 1, \qquad (8.11)$$

$$K_\theta = \mu_1' + \mu_2 |\dot{\theta}|,\ \ \mu_1' = \mu_1\sqrt{g^{-1}a}.$$

All the mentioned models have the symmetries, which are useful to account when analyzing the dynamic behavior.

(S1). Mirror symmetry: $u \to -u,\ v \to v,\ \theta \to -\theta,\ X \to -X,\ Y \to Y,\ \Gamma \to -\Gamma$.

(S2). Upheaval plate symmetry: $u \to -u,\ v \to -v,\ \theta \to \theta + \pi,\ X \to X,\ Y \to Y,\ \Gamma \to \Gamma$.

In the phase space of the system with symmetry for any object, like a regular or chaotic attractor, there are two possibilities [17]. The first is that the object itself is symmetric, i.e. with the corresponding change of variables it transforms to itself. The second option is that the object is asymmetric, then, the result of its transformation is a distinct object of the same nature, which is referred to as the symmetric partner of the original one.

8.2. Multistability and chaos in Kozlov model

Although the complex dynamics in a finite-dimensional description of the falling plate was reported first by Tanabe and Kaneko, it appears in a much simpler model, without account of the circulation and respective forces.

As noted in Section 3, in the integrable case $k_1 = k_2/(1+r)$ the Kozlov model (3.16) reduces to the pendulum equation with damping and shows only the regular dynamics. As we depart from the condition of integrability, the loss of stability of the fixed point of the steady fall is accompanied by the Andronov – Hopf bifurcation with appearance of the limit cycle of the first kind. It is responsible for periodic self-oscillations, flutter. The limit cycle initially is located roughly inside the separatrix (in terms of the reduced model), but under variation of parameters it can approach the separatrix, passing close to saddles; this creates preconditions for emergence of complex dynamics and chaos.

Fig. 19 shows a chart of regimes for the model (3.16) in the parameter plane (r, k_3) for fixed k_1=0.06 and k_2=0.3. The chart is obtained by scanning upward with inheritance. On the periphery of the chart phase portraits of the attractors are shown in projection on the plane of variables $(\theta, \dot{\theta})$. The dotted line on the chart corresponds to the threshold of stability loss of the fixed point (3.17).

When moving in the parameter plane from the bottom upward one observes, first, the bifurcation of symmetry break of the autorotation regime (passage from blue to green area), and then a sequence of period-doubling bifurcations with the transition to chaos. Initially, there is a non-symmetric chaotic attractor. Therefore, four attractors coexist here as symmetric partners with respect to the symmetry operations S1 and S2. Next, they merge into a single symmetric chaotic attractor. When varying parameters inside the area occupied mostly by chaos one observes narrow windows of periodicity. After exit from the complex dynamics region we arrive to the domain of periodic self-oscillations marked as dark blue on the chart, and after that to the black area of the stationary regime of steady fall. It should be noted that the border of these regions in the right part of the chart does not coincide with the line of stability loss; it is so due to the change of the Andronov – Hopf bifurcation nature (from supercritical, accompanied by soft creation or disappearance of a limit cycle in the left part of the chart, to subcritical, corresponding to hard transition and hysteresis in the right part of the chart).

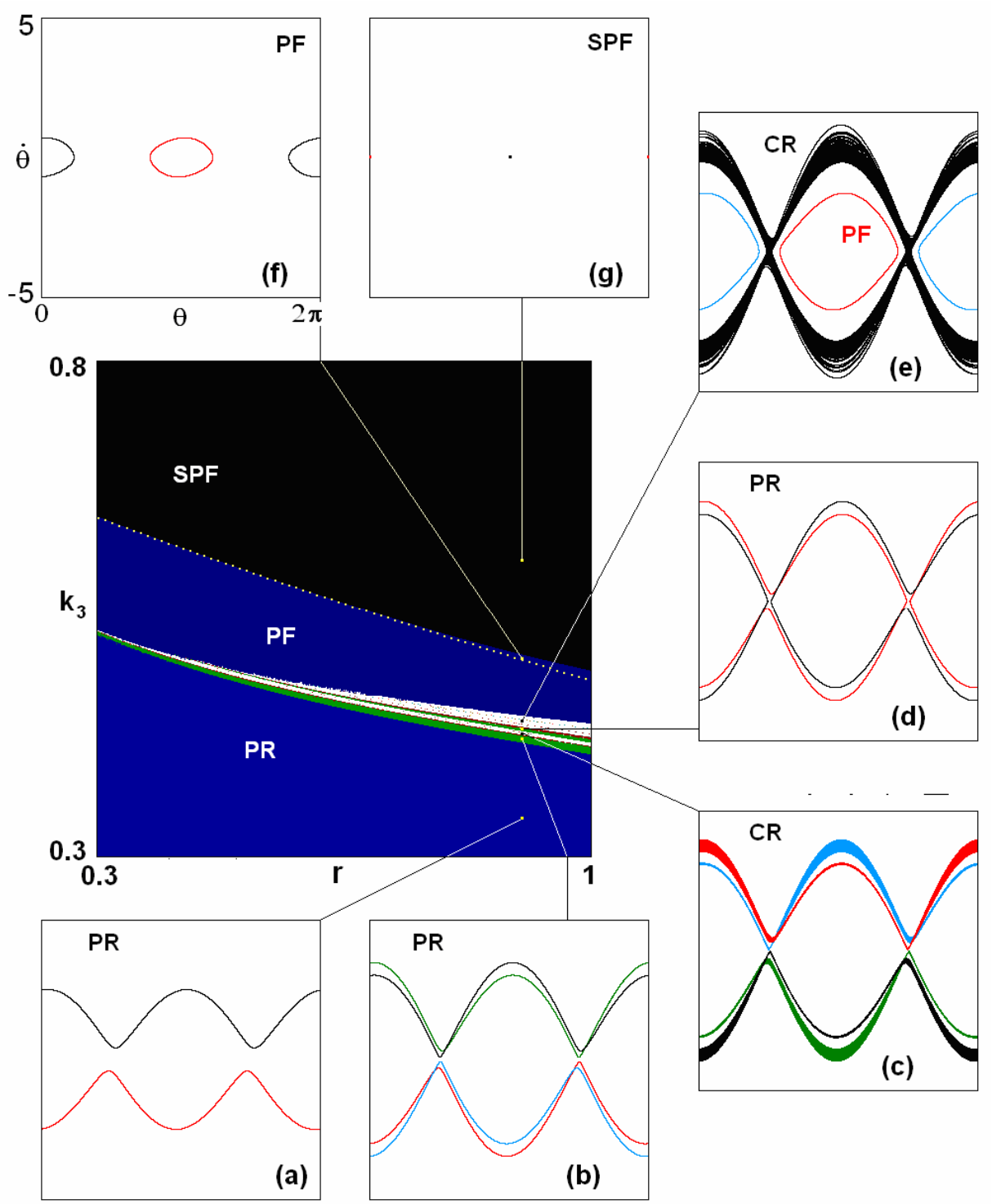

Figure 19: Chart of regimes for the model (3.16) for fixed k_1=0.06 and k_2=0.3 obtained by scanning the parameter plane (r, k_3) upward with inheritance, and phase portraits of attractors in projection onto the plane $(\theta, \dot{\theta})$ at representative points. Attractors, which are symmetric partners with respect to S1 and S2 are drawn in different colors. The domain PR corresponds to periodic autorotation, PF – to periodic oscillations (flutter), SPF – to the plate fall without oscillations. Symbols CR and CF on the phase portraits designate the chaotic regimes of rotation and flutter. The dotted line corresponds to threshold of the stability loss for the fixed point (3.17).

Figure 20 shows phase portraits of attractors to compare them with attractors for Tanabe – Kaneko models in Fig. 13; observe the visually similar forms. Attractor in the diagram (a) is the limit cycle arisen after the symmetry break bifurcation and two period-doubling bifurcations. The diagram (b) shows a chaotic attractor formed as a result of a cascade of period doubling

bifurcations. As it is asymmetric, we can be sure that symmetric partners coexist, which are generated by the symmetry operations S1 and S2. The diagram (c) shows a symmetric chaotic attractor, which may be interpreted as a result of unification of those symmetric partners into a single object. Lyapunov exponents of the attractors calculated by solving the system (3.16) and the corresponding variation equations with the Benettin algorithm [18.14,15] are given in the figure caption.

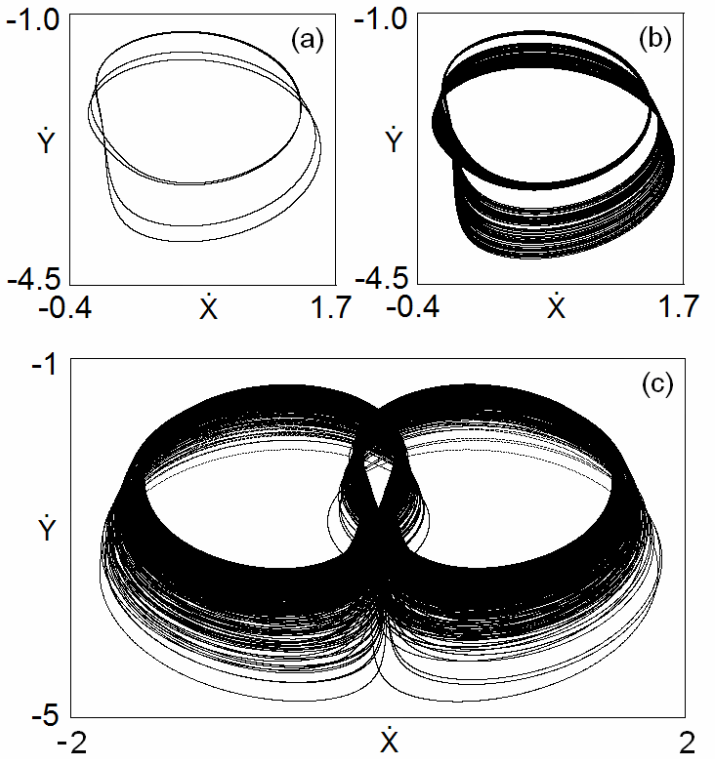

Figure 20: Phase portraits of attractors for Kozlov model with k_3=0.423 (a), 0.424 (b), 0.437 (c). Other parameters are r=0.9, k_1=0.06, k_2=3. Dimensionless components of the translational velocity in the laboratory frame are plotted along the coordinate axes: $\dot{X} = u\cos\theta - v\sin\theta$, $\dot{Y} = u\sin\theta + v\cos\theta$. The Lyapunov exponents are $\{0, -0.089, -0.326, -2.106\}$ (a), $\{0.091, 0, -0.326, -2.272\}$ (b), $\{0.186, 0, -0.341, -2.398\}$ (c).

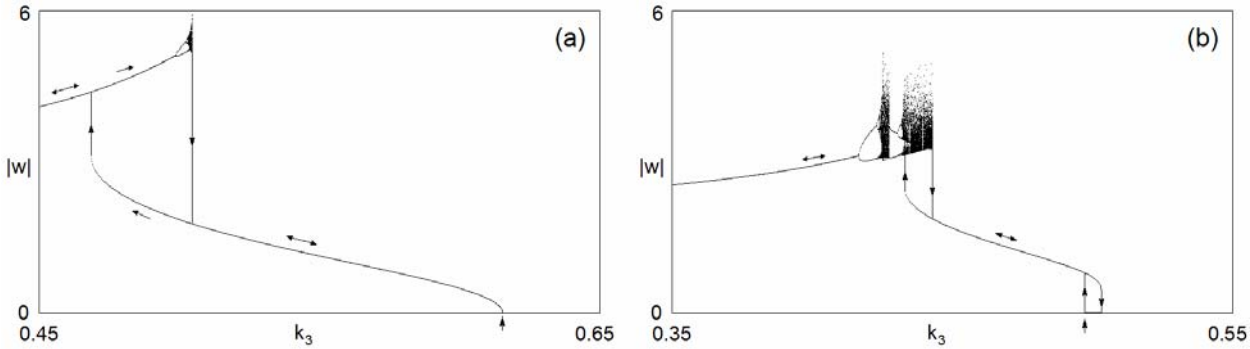

Figure 21: One-parameter bifurcation diagrams obtained in computations for the Kozlov model (3.16) with k_1=0.06, k_2=3, r=0.4 (a) и r=0.9 (b). The directions of variation of the parameter are indicated by the arrows at the branches of the diagrams. The vertical arrow below the x-axis marks the point of stability loss for the steady fall according to (3.17).

To visualize multistability let us turn to a one-parameter bifurcation diagram. In Fig. 21, the absolute value of the angular velocity is plotted versus the parameter of viscous friction for the rotational motion. In computations this parameter k_3 is increased (decreased) step by step, the initial conditions are used corresponding to the final state at the previous step. The branches obtained with scanning from left to right and from right to left are indicated with respectively directed arrows. The difference between regimes observed in the one and the other case indicates the presence of coexisting distinct attractors at the same parameters, each of which has its own

basin in the state space that is a set of initial points, starting from which the phase trajectories arrive finally to this attractor. This is the hysteresis effect. We emphasize that the attractors coexisting here are not symmetric partners with respect to the symmetry operations S1 and S2.

The diagram (a) demonstrates a single region of bistability, wherein one of the coexisting attractors is a limit cycle corresponding to periodic flutter, and the second corresponds to periodic (in the left part of the interval) or chaotic (the right part of the interval) autorotation. At the point marked with arrow below the horizontal axis an Andronov – Hopf bifurcation occurs of the limit cycles birth, which is normal (supercritical).

The diagram (b) shows two parameter intervals of bistability. In one of them, on the left side of the figure, attractors coexist associated with periodic flutter (lower branch) and with chaotic autorotation (upper branch). In the second interval placed to the right, a limit cycle corresponding to periodic self-oscillations coexists with a stable fixed point corresponding to a steady fall. Here the Andronov – Hopf bifurcation of stability loss of the fixed point is subcritical [44, 45, 19].

8.3. Modified Tanabe – Kaneko model

The modification of the Tanabe – Kaneko model discussed in Subsection 8.1 leads to equations

$$\begin{aligned} \dot{u} &= v\dot{\theta} + 2rv^2 \operatorname{sgn} u - \sin\theta - rk_1 u, \\ (1+r)\dot{v} &= (r-1)u\dot{\theta} - 2ruv \operatorname{sgn} u - \cos\theta - rk_2 v, \\ (\tfrac{1}{4} + \tfrac{1}{8}r)\ddot{\theta} &= -ruv - rk_3\dot{\theta}. \end{aligned} \qquad (8.12)$$

Selecting appropriate value of r it is possible to achieve rather a good agreement of the dynamics in the modified and the original equations ((8.12) and (5.1), respectively). [4]

Figure 22 shows a chart of regimes of the model (8.12) in the parameter plane $(k_2,\ f = k_2/k_1)$ at $k_3 = k_2/4$ and r=0.1. It can be compared with the chart of the original system Tanabe – Kaneko in Figure 11. As seen, the charts look very similar. (The scales of the figures are chosen to make clear the visual comparison, although normalizations of the equations (8.12) and (5.1) are different.) In both versions of the model, there are similar regimes, and obvious correspondence in mutual placement of domains of different regimes in the parameter plane is observed. Figure 23 shows phase portraits of attractors for model (8.12) at $f = k_2/k_1 = 100,\ k_3 = k_2/4$ for a number of values k_2 that look similar to attractors of the original model in Figure 13.

Bearing in mind subsequent comparison with the Anderson – Pesavento – Wang model, consider the chart of regimes in the parameter plane (r, k_3) for fixed values of k_1 and k_2.The chart shown in Fig.24 was obtained by scanning upward with inheritance. On the periphery of the figure phase portraits of attractors are shown, and those coexisting at identical parameters are drawn in different colors.

Moving upward in the parameter plane (i.e., with increase of the dissipation parameter) in the left side of the chart the first observed is bifurcation of symmetry break of the autorotation (transition from blue to green region), then the sequence of period doubling bifurcations follows with the transition to chaos. Initially, the arisen chaotic attractor is asymmetric, and together with it there are symmetric partners with respect to the S1 and S2 symmetries. With further parameter increase they merge into a single symmetric chaotic attractor. Inside the complex dynamics

---

[4] Equation (5.1) by a change of the variables and parameters $v_x = u\sqrt{2gl/3},\ v_y = v\sqrt{2gl/3},\ t = \tau\sqrt{2l/3g}$, $rk_1 = k_{\|}\sqrt{2l/3g},\ rk_2 = k_{\perp}\sqrt{2l/3g},\ 4rk_3 = k_{\perp}\sqrt{2l/3g}$, reduce to the form $\dot{u} + k_1 u = \dot{\theta}v - \sin\theta + \frac{2}{3}\pi\bar{\rho}lv\operatorname{sgn} u$, $\dot{v} + k_2 v = -\dot{\theta}u - \cos\theta - \frac{2}{3}\pi\bar{\rho}luv\operatorname{sgn} u,\ \ddot{\theta} + k_3\dot{\theta} = -\frac{4}{3}\pi\bar{\rho}luv$. If we assume that $r = \frac{1}{3}\pi\bar{\rho}l$ and take parameters as those in [23] it gives $r \approx 0.1$, and the above expressions are very similar to (8.12), with only difference in the nearly unity coefficients $1+r,\ 1-r,\ 1+r/2$. Therefore, the dynamics of models (5.1) and (8.12) are similar, and it is observed in the computations.

domain occupied mostly by chaos, narrow windows of periodicity occur that can correspond either flutter or autorotation.

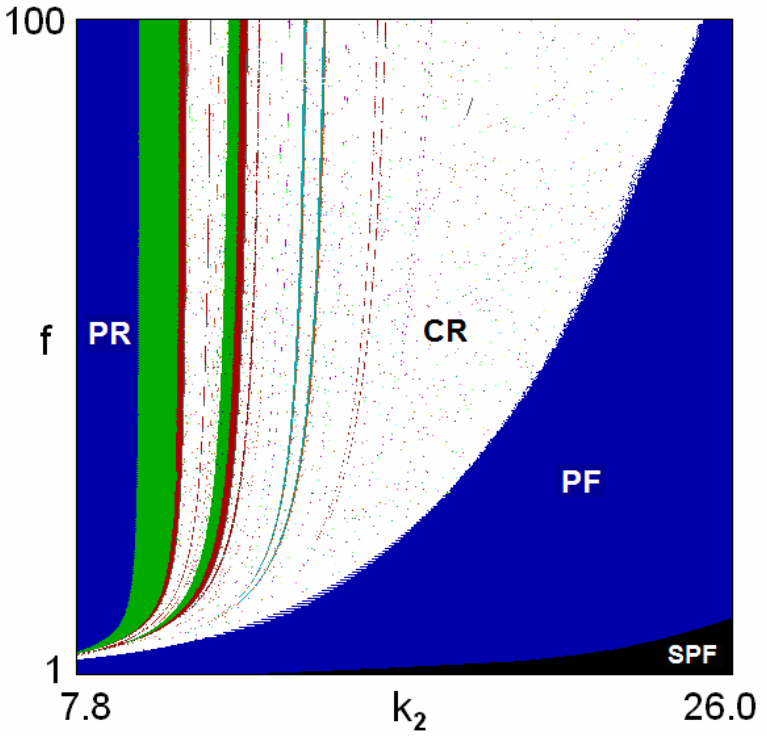

Figure 22: Chart of regimes of the modified Tanabe – Kaneko model (8.12) for r=0.1 at $k_1 = k_2 / f$ $k_3 = k_2 / 4$ on the parameter plane (k_2, f). The colors are determined by a repetition period for the squared angular velocity in the Poincaré section. Period 1 regimes with and without symmetry are shown in blue and green, respectively; other colors correspond to larger periods. White areas represent chaos or unrecognized high-period regimes. Inscriptions mean periodic rotation (PR), chaotic rotation (CR), and periodic flutter (PF). Black color designates simple perpendicular fall (SPF).

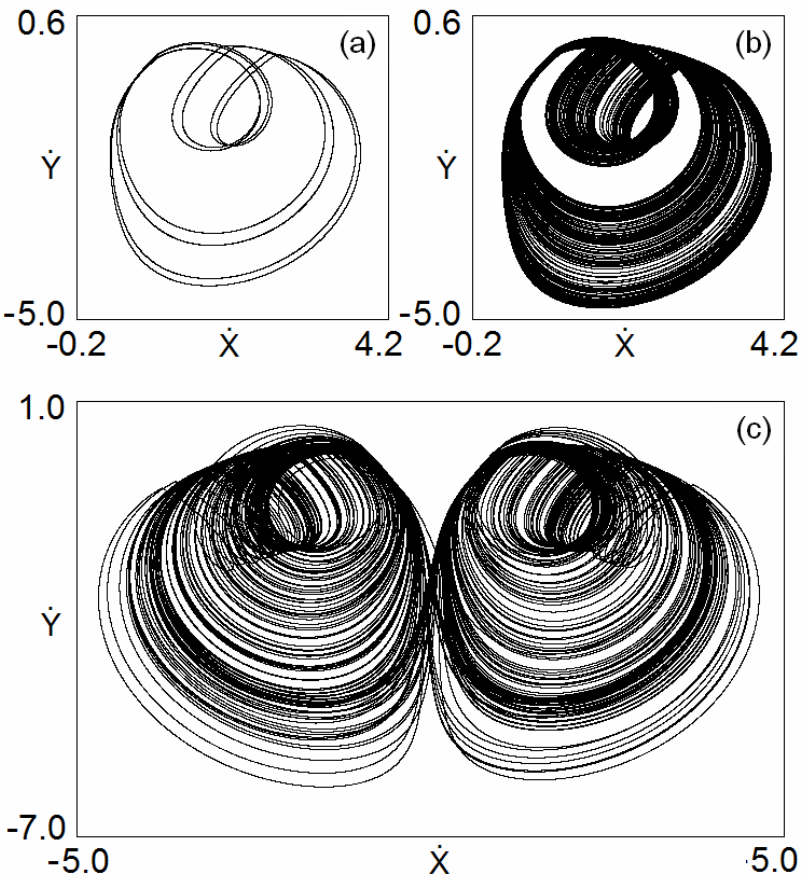

Figure 23: Phase portraits of attractors of the model (8.12) with $k_2 = 10.86$ (a), 11 (b). 11.6 (c), $k_1 = k_2 / 100$, for $r = 0.1$. Along the coordinate axes dimensionless velocity components in the laboratory frame are plotted. Lyapunov exponents: $\{0, -0.029, -0.359, -1.906\}$ (a), $\{0.043, 0, -0.435, -1.862\}$ (b), $\{0.098, 0, -0.488, -1.757\}$ (c).

In the right part of the chart, the exit from the area of periodic dynamics upward is accompanied by a rigid transition and hysteresis. In particular at the point (0.95, 0.1) periodic regimes of autorotation and flutter coexist. When moving in the parameter plane in the opposite direction (from top to down), we observe initially the periodic oscillations (flutter), which correspond to a limit cycle of the first kind (dark blue area in the upper right corner of the chart). Gradually, the limit cycle increases in size and at some place, obviously connected with the approach to the saddle, its topological nature is changing, and it turns into a limit cycle of the second kind corresponding to autorotation (the area indicated a lighter blue). Then this cycle loses symmetry (transition from blue to green region), and after that the cascade of period-doubling bifurcations for autorotation regimes occurs with transition to chaotic tumbling regime.

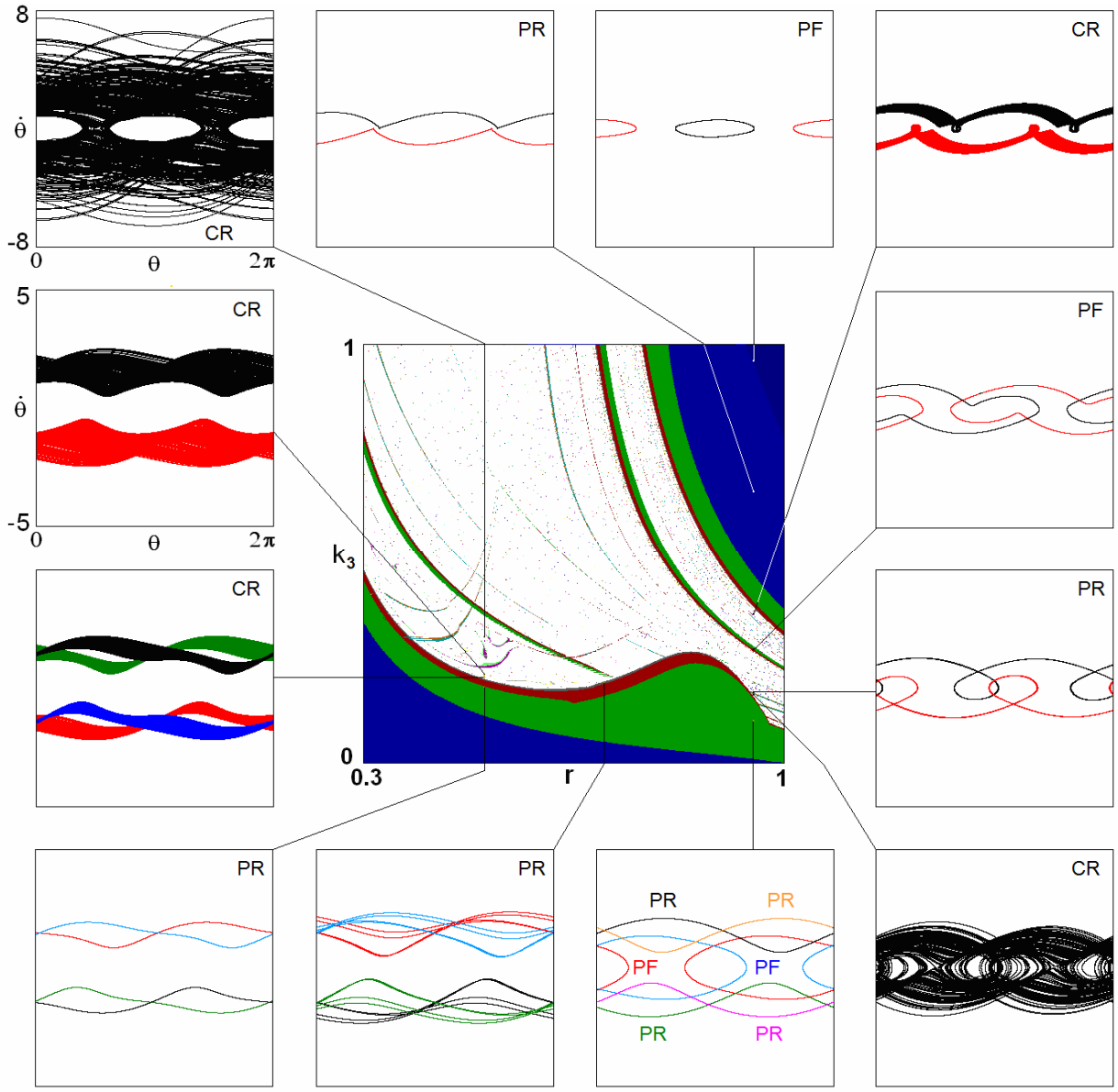

Figure 24: Chart of regimes for the modified Tanabe – Kaneko model (8.12) on the parameter plane r, k_3 with $k_1 = 0.06$, $k_2 = 3$. On the periphery of the figure portraits of attractors are shown at representative points corresponding to periodic rotation PR, chaotic rotation CR, periodic flutter PF, chaotic flutter CF. The colors are determined by a repetition period for the squared angular velocity in the Poincaré section. Period 1 regimes with and without symmetry are shown in blue and green, respectively. Other colors correspond to larger periods. White areas represent chaos or unrecognized high-period regimes.

8.4. Modified Belmonte – Eisenberg – Moses model

Equations for the modified Belmonte – Eisenberg – Moses read

$$\dot{u} = v\dot{\theta} + 2rv^2 \operatorname{sgn} u - \sin\theta - \alpha_{\|} r\sqrt{u^2+v^2}\,u,$$
$$(1+r)\dot{v} = (r-u)\dot{\theta} - 2ruv \operatorname{sgn} u - \cos\theta - \alpha_{\perp} r\sqrt{u^2+v^2}\,v, \qquad (8.13)$$
$$(\tfrac{1}{4}+\tfrac{1}{8}r)\ddot{\theta} = -ruv - \alpha_{\omega} r\,|\,\dot{\theta}\,|\,\dot{\theta}.$$

Fig. 25 shows chart of regimes for the model (8.13) in the parameter plane (r, α_ω) obtained by scanning from left to right with inheritance. On the periphery portraits of attractors are shown at some representative points in the projection on the plane $(\theta, \dot{\theta})$. Attractors coexisting at identical parameters are drawn in different colors. Inscriptions on the map are explained in the caption and correspond to nomenclature of Tanabe and Kaneko.

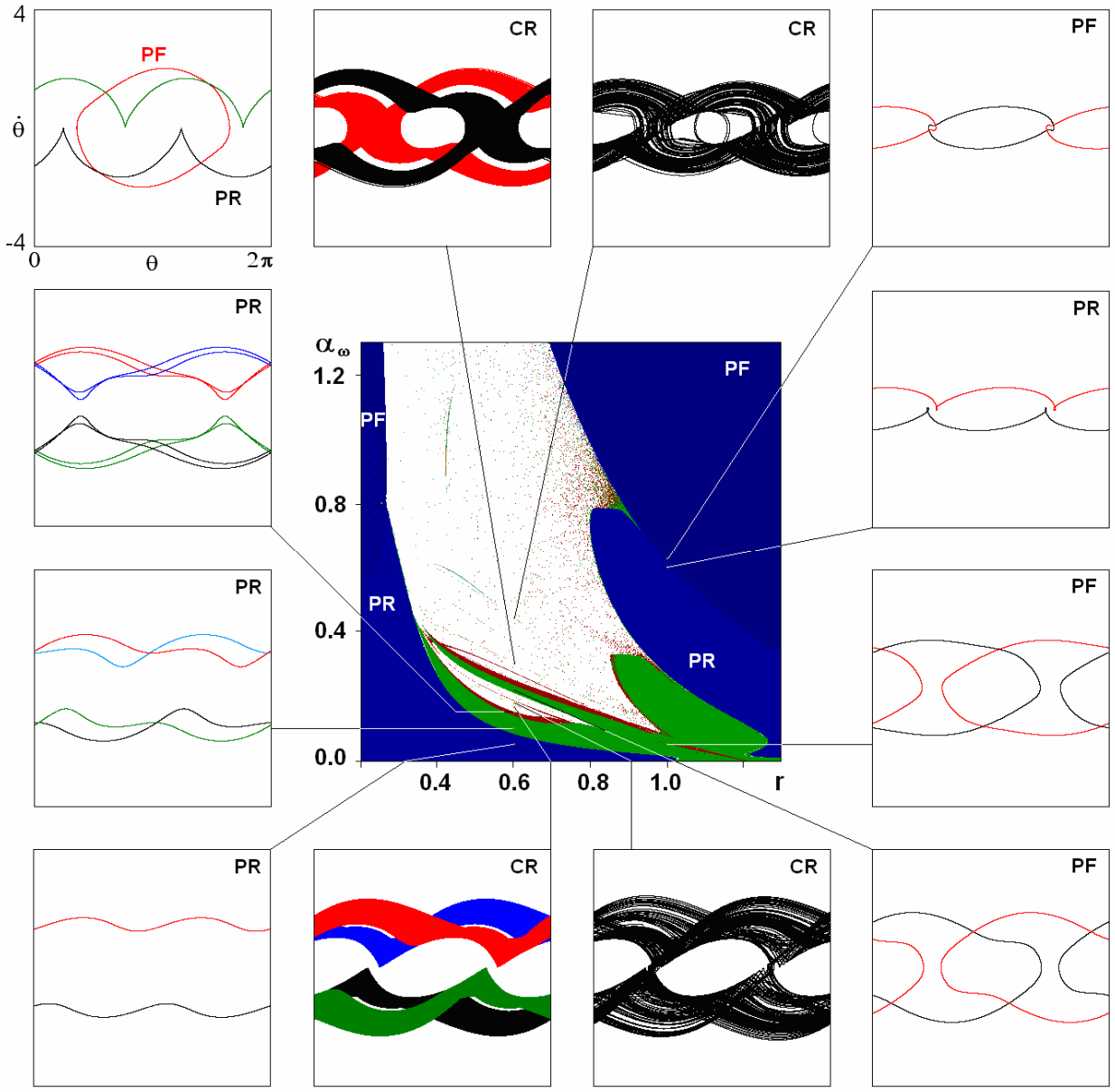

Figure 25: Chart of regimes for the model (8.13) with $\alpha_{\|} = 0.14$, $\alpha_{\perp} = 0.65$ and phase portraits of attractors in the projection onto the plane $(\theta, \dot{\theta})$ at representative points corresponding to periodic rotation PR, chaotic rotation CR, periodic flutter PF, chaotic flutter CF. The colors are determined by a repetition period for the squared angular velocity in the Poincaré section. Period 1 regimes with and without symmetry are shown in blue and green, respectively. Other colors correspond to larger periods. White areas represent chaos or unrecognized high-period regimes.

Attractors for regimes of periodic flutter PF and periodic autorotation PR demonstrate a visual similarity with the portraits in Fig. 16. However, a quantitative comparison of the modified model (8.13) with the original Belmonte – Eisenberg – Moses model (6.4) appears to be not legitimate. As can be shown, the Froude number determined according to [26] and expressed in terms of parameters of the model (8.13) is $\mathrm{Fr} = \sqrt{\pi / r}$, so at parameters used in Figs. 15 and 16 the Froude numbers 0.89 and 0.45 correspond to large values of r (about 4 and 15). This corresponds to very significant contribution of added masses, which are not accounted in the equations (6.4).

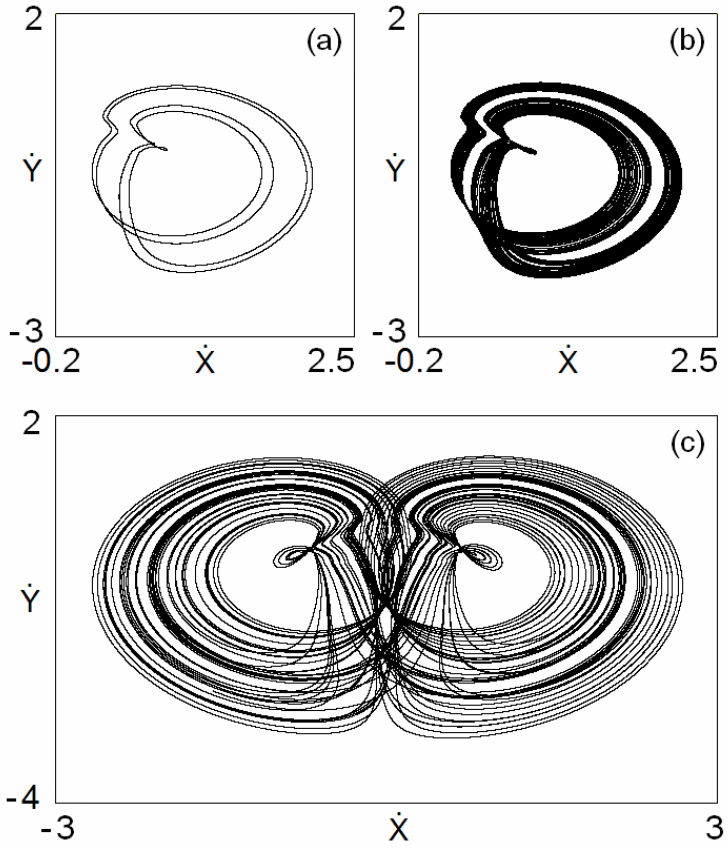

Figure 26: Phase portraits of attractors for model (8.13) with r=0.6 и a_w=0.157 (a), 0.16 (b), 0.2. Along the coordinate axes dimensionless components of the translational velocity in the laboratory frame $\dot{X} = u\cos\theta - v\sin\theta$, $\dot{Y} = u\sin\theta + v\cos\theta$ are plotted. The Lyapunov exponents are $\{0, -0.042, -0.337, -1.493\}$ (a), $\{0.037, 0, -0.414, -1.516\}$ (b), $\{0.133, 0, -0.526, -1.726\}$ (c).

8.5. Anderson – Pesavento – Wang model compared with others

As noted, the Anderson – Pesavento – Wang model [28] is the most elaborated finite-dimension model for description of fall of the plate in a resisting medium. When using normalization adopted in the present Section, the equations (7.3) can be rewritten as

$$\begin{aligned} \dot{u} &= (1-r)v\dot{\theta} - \frac{2ru^3}{5\pi\sqrt{u^2+v^2}} - \sin\theta, \\ (1+r)\dot{v} &= (2r-1)u\dot{\theta} - r\frac{14u^2+12v^2}{5\pi\sqrt{u^2+v^2}}v - \cos\theta, \\ (\tfrac{1}{4}+\tfrac{1}{8}r)\ddot{\theta} &= -ruv - r(\mu_1 + \mu_2 |\dot{\theta}|)\dot{\theta}, \end{aligned} \qquad (8.14)$$

where $r = 1/I^*$. Having in mind comparison with other models, it is natural to study the dynamics in dependence on parameters which are present both in (8.14) and in the models subjected to the comparison. In this connection, we use r as one variable parameter, and the

coefficient of linear or quadratic rotation resistance force in the third equation as another one. With regard to the first two equations, their form and coefficients will be assumed unchanged.

In the normalization we use now, the loss of stability for steady fall occurs at the critical coefficient of friction

$$\mu_1 = \mu_* = \frac{1}{4}\sqrt{\frac{3}{5\pi r}\,\frac{2+r}{1-r}}\,. \qquad (8.15)$$

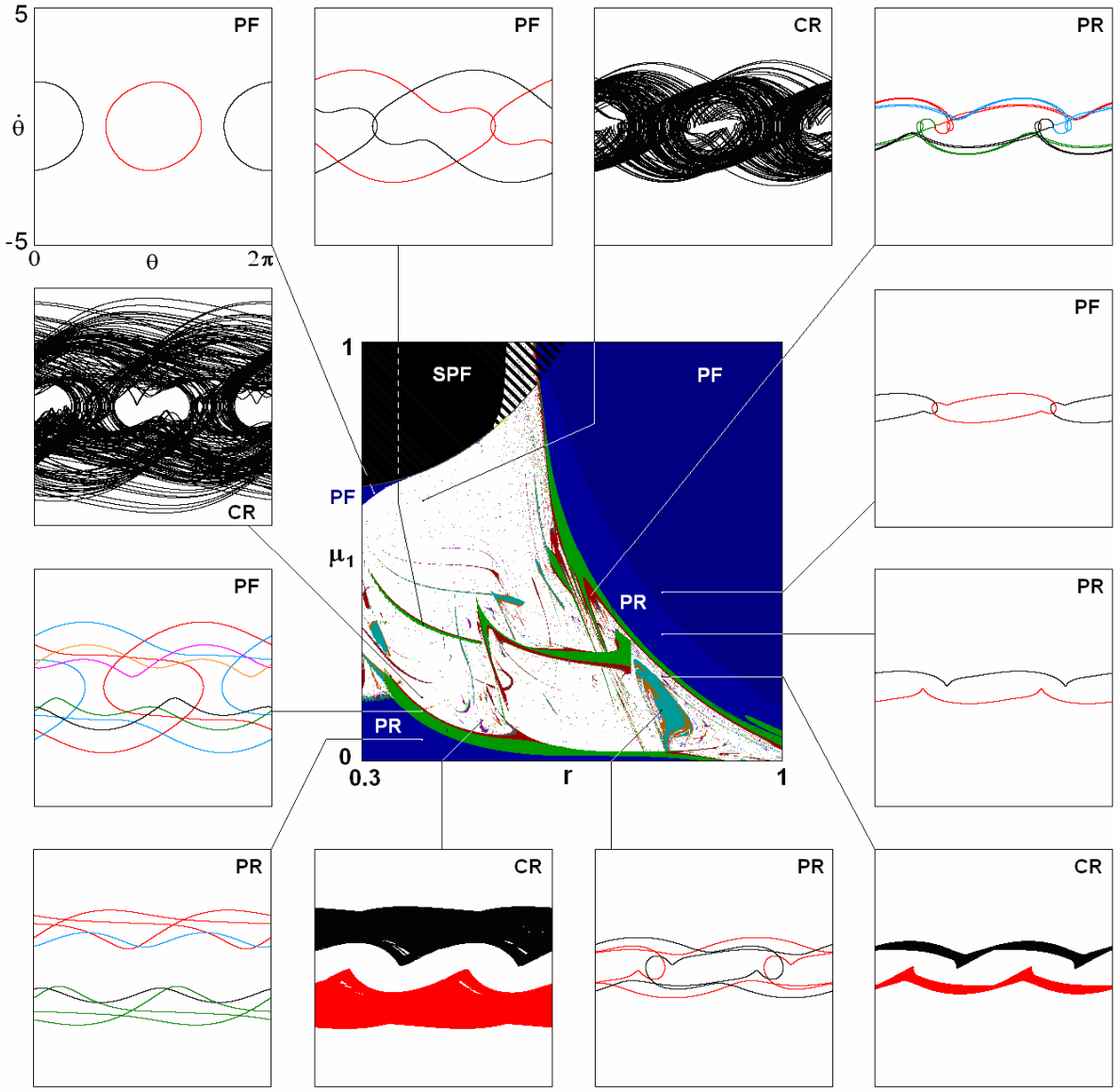

Figure 27: Chart of regimes for the model (8.14) with μ_2=0, obtained by upward scanning with inheritance, and phase portraits of attractors at representative points. Attractors coexisting at identical parameters are shown in different colors. PR means periodic autorotation, PF – periodic flutter, SPF – steady perpendicular fall. Inscriptions CR and CF relate to chaotic regimes of rotation and flutter. Inclined stripes on the right side of the SPF area designated coexistence of autorotation or flutter regimes with the steady fall.

Figure 27 shows a chart of regimes on a plane of viscous friction coefficient μ_1 and parameter r in the absence of the quadratic resistance force for rotation (μ_2=0). Figure 28 provides a chart on a plane of the quadratic friction coefficient μ_2 and the parameter r without viscous friction (μ_1=0). Both charts are obtained by scanning upward with inheritance. Inscriptions on the charts and portraits of attractors follow the nomenclature of Tanabe and Kaneko: PR and CR designate, respectively, periodic and chaotic autorotation, PF means

periodic flutter oscillations, SPF is simple perpendicular fall of the plate without oscillations. On the periphery of the figure phase portraits of attractors are shown.

The chart on Fig. 27 is appropriate for comparison of the results with the Kozlov and Tanabe – Kaneko models, and the chart on Fig. 28 is suitable for comparison with the model of Belmonte, Eisenberg and Moses.

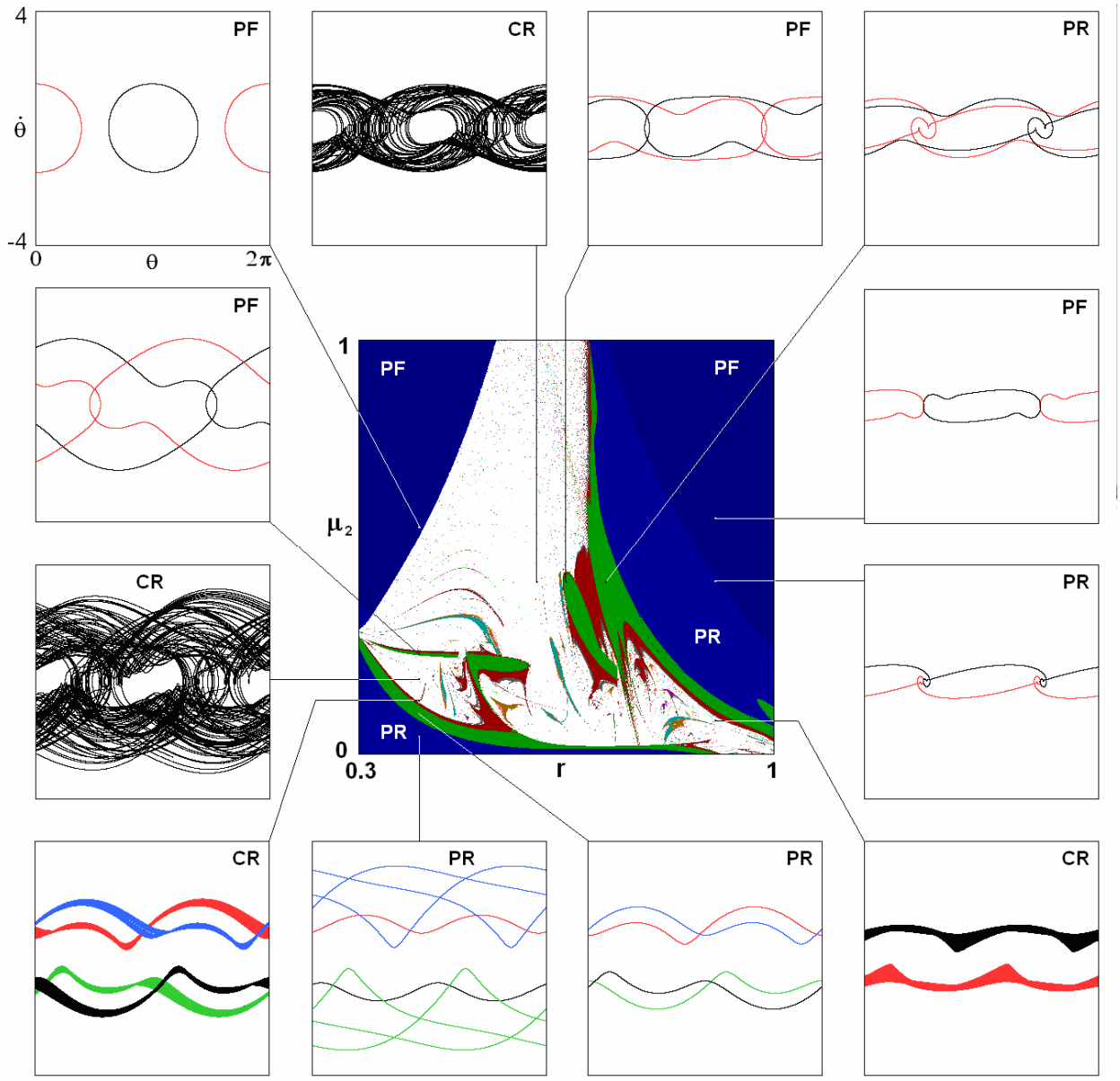

Figure 28: Chart of regimes for the model (8.14) with μ_1=0, obtained by scanning the parameter plane (r,μ_2) upward with inheritance, and phase portraits of attractors at representative points. Designation and inscriptions are similar to the previous figure.

In addition to the Anderson – Pesavento – Wang model, it is interesting to consider its approximate version, using circulation and resistance forces in the assumption that the longitudinal translational motion of the plate is characterized by a much greater velocity than the orthogonal component. In the limit case $|u|>>|v|$ the circulation is given by the expression

$$\overline{\Gamma} = -\frac{12}{5\pi}\operatorname{sgn} u + 2\dot{\theta} = -0.76\operatorname{sgn} u + 2\dot{\theta}\,. \qquad (8.16)$$

In structure it is similar to the formula (8.9) from Sedov book [9] based on the Kutta – Joukovsky – Chaplygin postulate used in the modified Tanabe – Kaneko and Belmonte –

Eisenberg – Moses models (8.12) and (8.13). Note, however, a difference in the numerical coefficients: instead of 2 and 1 in (8.9) the expression (8.16) contains the constants 0.76 and 2.

The resistance force coefficients for the translational motion are expressed in this approximation as

$$K_{x,y} = \frac{2}{5\pi}\sqrt{u^2+v^2} = 0.13\sqrt{u^2+v^2} \tag{8.17}$$

that differs from the Belmonte – Eisenberg – Moses in the numeric constants. (Instead of 0.14 and 0.65 for the longitudinal and transversal motion we have one and the same coefficient 0.13).

The dynamical equations for this limit case of Andersen – Pesavento – Wang model may be written as

$$\begin{aligned} \dot{u} &= (1-r)v\dot{\theta} - \tfrac{2}{5\pi} r u^2 \operatorname{sgn} u - \sin\theta, \\ (1+r)\dot{v}_y &= (2r-1)u\dot{\theta} - \tfrac{14}{5\pi} ruv \operatorname{sgn} u - \cos\theta, \\ (\tfrac{1}{4}+\tfrac{1}{8}r)\ddot{\theta} &= -ruv - r(\mu_1' + \mu_2 |\dot{\theta}|)\dot{\theta}. \end{aligned} \tag{8.18}$$

Fig. 29 shows the chart of regimes in the plane of parameter r and the coefficient of viscous resistance for rotational motion of the body μ_1. Panel (a) corresponds to the Anderson – Pesavento – Wang model (8.14), and (b) to the approximate version of this model (8.18). Panel (c) relates to the modified Tanabe – Kaneko model (8.12).

Fig. 30 shows the chart of regimes in the plane of parameter r and the factor of quadratic resistance force for rotational motion; the viscous friction is absent $(\mu_1 = 0)$. As in the previous figure, panels (a) and (b) refer to the Anderson – Pesavento – Wang model (8.14) and to the limit case of this model (8.18). Panel (c) corresponds to the modified Belmonte – Eisenberg – Moses model (8.13).

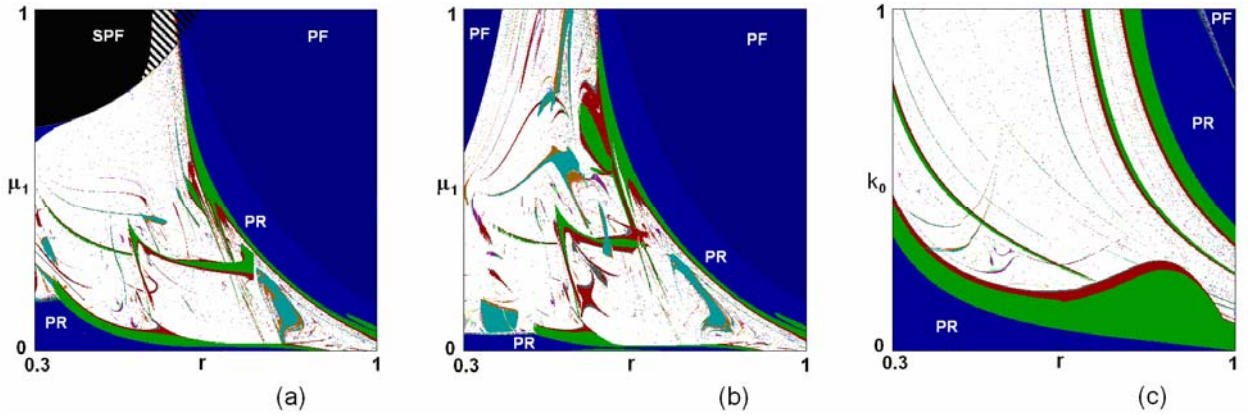

Figure 29: Comparison of charts of regimes for Andersen – Pesavento – Wang model (a), the limit case of this model (b), and for the modified Tanabe – Kaneko model (c).

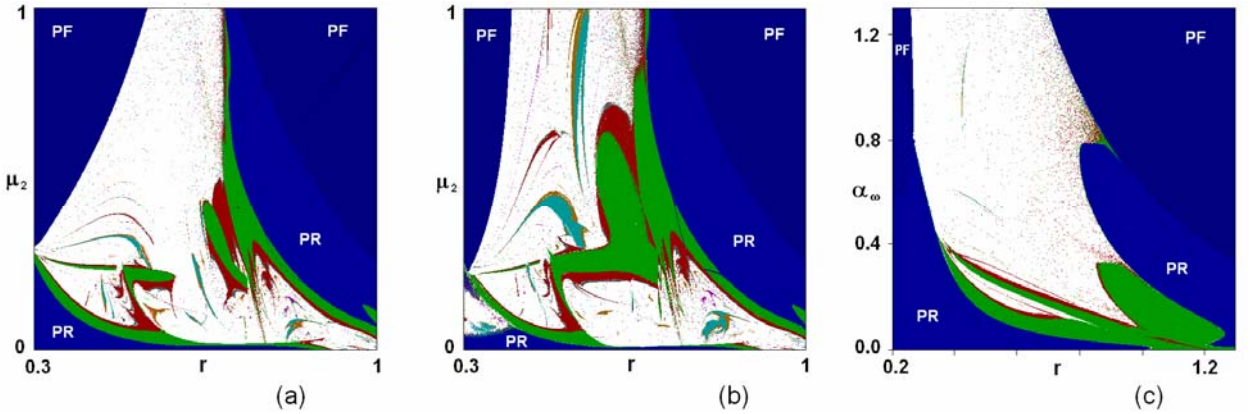

Figure 30: Comparison of charts of regimes for Andersen – Pesavento – Wang model (a), the limit case of this model (b), and for the modified Belmonte – Eisenberg – Moses model (c) i.

Comparing panels (a) and (b) in Fig. 29 and 30 one observes that the general structure of the regions in the parameter space is analogous, although relative size and placement of the formations vary. This observation supports legitimacy of use of circulation formula within the Kutta – Joukovsky – Chaplygin postulate at least in a level of qualitative analysis.

Less expressed but noticeable similarities are seen between diagrams (b) and (c) in both figures. Note the presence of regions PF in the upper right corner of the charts and PR in the lower left corner while chaotic dynamics occupies in the central part of the charts. One more common feature is the transition to chaos through the period doubling cascade preceded by the symmetry break bifurcation in the bottom left part of the carts. Thus, despite some quantitative difference, the whole picture of the dynamics on the base of the considered models looks quite recognizable and consistent. Obviously, this is so because of common underlying conservative dynamics (Kirchhoff equations), due to common properties of symmetry, and due to universal nature of the involved phenomena of nonlinear dynamics (fixed points, limit cycles, attractors, bifurcations).

Conclusion

The article reproduces results of studies of the plane problem of the fall of the plate in a resisting medium based on models in the form of ordinary differential equations for a relatively small number of variables, and provides comparative analysis of these models. Methodological basis for the finite-dimensional description is the fact that in the case of an ideal incompressible non-viscous fluid the generalized coordinates and velocities of the rigid body are governed by Kirchhoff equations separated from the equations relating to fluid.

As a part of the review we tried to draw a line of reasoning, starting from a situation where the Kirchhoff equations are reduced to the pendulum equation with sinus nonlinearity to models showing self-oscillatory and autorotation periodic or chaotic regimes by taking into account certain assumptions concerning forces acting on the body from the viscous medium. Similar approach is proved to be fruitful in theory of oscillations, when a conservative oscillator is used as a starting model for subsequent modifications involving damping of the oscillations, excitation of self-oscillations, and occurrence of chaotic dynamics.

In the problem of falling body in a resisting medium, the periodic oscillations – flutter and periodic motion with tumbling – autorotation are interpreted as those associated with the limit cycles of the first and the second kind in the phase space (more precisely, in the subspace of the generalized velocities).

To study the problem of the body fall in fluid we apply concepts and toolbox of nonlinear dynamics, including visualization of the dynamical phenomena by portraits of attractors, consideration of Poincaré recurrence maps, mapping dynamic regimes in the parameter plane (charts of dynamical regimes), analysis of bifurcation diagrams ("trees"), computation of spectra of Lyapunov exponents. This made it possible to fulfill the picture of the dynamics uncovered on the basis of finite-dimensional models with broad illustrative material.

It is found and deserves attention an unexpected richness of dynamic behavior exhibited by the simplest model [22], where only linear viscous resistance of translational and rotational motion of the body are taken into account while the circulation and related effects like the lifting force are ignored. Previously, attention was focused only on simple regimes of dynamics of this model, but in a certain ranges of parameters rather complex phenomena such as chaos, cascade of period-doubling bifurcations, multistability are possible.

An original result is discovery of the Lorenz-type strange attractor in three-dimensional space of generalized velocities for the problem of motion of elliptic profile in the conditions of compensated gravity, in the presence of viscous friction, with constant velocity circulation around the profile, and with external applied to the body constant torque.

With respect to the Tanabe – Kaneko model, which takes into account the effect of lift on the moving profile according to the Kutta – Joukovsky – Chaplygin postulate, the undertaken analyzes includes reproduction of results of the original work, modification of the model taking

into account the criticism it was subjected to, and comparison of the original and the modified model. It reveals that, despite seemingly significant deficiencies, the model qualitatively gives a reasonable general picture of possible phenomena of complex dynamics for the fall of the plate in fluid, at least in a certain range of parameters. A similar study was carried out in relation to the Belmonte – Eisenberg – Moses model assuming that the friction is quadratic in the generalized velocities.

For the Anderson – Pesavento – Wang model, based on proposed empirical formulas for the drag and lift forces, an extensive numerical material is presented, including charts of regimes in the parameter space.

We introduce a generalized model using common dimensionless variables and parameters and provide comparative analysis of the dynamic behavior of the Kozlov, Tanabe – Kaneko, Belmonte – Eisenberg – Moses and Andersen – Pesavento – Wang models.

It is worth noting important role of symmetry of the problem of the plate fall in fluid for understanding the inherent phenomenology of complex dynamics. In particular, a relevant feature is a possibility of coexistence of attractors, which are mutually symmetrical objects, and a possibility of combining them into a single attractor under variation of control parameters.

We conclude that the overall structure of the parameter space for different models shows certain similarities. Thus, despite the quantitative difference, picture drawn on the basis of the considered models for the falling plate in a resisting medium appears to be quite consistent. This fact is obviously determined by common underlying conservative dynamics (Kirchhoff equation). Its modification with account of the effects of viscosity has general features due to the inherent symmetry and to the universal nature of the involved phenomena of nonlinear dynamics (fixed points, limit cycles, attractors, bifurcations).

I would like to express thanks to A.V. Borisov who called my attention to the issues discussed in this paper.

References

1. Maxwell J. C. On a particular case of the descent of a heavy body in a resisting medium //Camb. Dublin Math. J., 1854, vol. 9, pp. 145-148.
2. Kirchhoff G.R. Über die Bewegung eines Rotationskörpers in einer Flüssigkeit //Ges. Abhandl. Leipzig: Johann Ambrosias Barth, 1882. S. 376—403.
3. Joukovsky N.E. On soaring birds. Collected Works. Vol. 4. Moscow: Gostekhizdat, 1949. P. 5-34. (In Russian.)
4. Belmonte A., Moses E. Flutter and tumble in fluids //Physics world, 1999, pp. 21-25.
5. D.L. Finn. Falling Paper and Flying Business Cards //SIAM News, 2007, vol. 40, no. 4.
6. Ern P., Risso F., Fabre D., Magnaudet J. Wake-induced oscillatory paths of bodies freely rising or falling in fluids //Annual Review of Fluid Mechanics, 2012, vol. 44, pp. 97-121.
7. Lamb H. Hydrodynamics. 6-th edition. Cambridge: Campridge University Press, 1993. 768p.
8. Borisov A.V., Mamaev I.S. Dynamics of rigid body. Moscow – Izhevsk: Institute of Computer Science, 2005, 576p. (In Russian.)
9. Sedov L.I. Two-dimensional problems in hydrodynamics and aerodynamics. N.Y., London, Sydney: John Wiley & Sons, 1965. 427p.
10. Kochin N.E., Kibel I.A. and Roze N.V. Theoretical Hydromechanics. John Wiley & Sons: Chichester, 1964, 583p.
11. Birkhoff G. Hydrodynamics: a study in logic, fact and similitude. Princeton University, 1950. 184p.
12. Arjannikov N.S., Sadekova G.S. Aerodynamics of aircrafts. Vysshaya Shkola, Moscow, 1983, 359p. (In Russian.)
13. Strange attractors /Sinai Ya.G. and Shil'nikov L.P. Moscow: Mir, 1981. 256c. (In Russian.)
14. Schuster H.G. and Just W. Deterministic chaos: an introduction. Wiley-VCH, 2005. 312p.
15. Kuznetsov S.P. Dynamical chaos. 2-nd ed. Moscow: Fizmatlit, 2006, 356p. (In Russian.)

16. Kuznetsov A.P., Kuznetsov S.P., Sataev I.R., Chua L.O. Multi-parameter criticality in Chua's circuit at period-doubling transition to chaos //International Journal of Bifurcation and Chaos, 1996, vol. 6, no 1, pp. 119-148.
17. Borisov A.V., Jalnin A.Yu., Kuznetsov S.P., Sataev I.R., Sedova J.V. Dynamical phenomena occurring due to phase volume compression in nonholonomic model of the rattleback //Regular and Chaotic Dynamics, 2012, vol. **17**, no 6, pp. 512-532.
18. Benettin G., Galgani L., Giorgilli A., Strelcyn J.-M. Lyapunov characteristic exponents for smooth dynamical systems and for Hamiltonian systems: A method for computing all of them //Meccanica, 1980, vol. **15**, pp. 9-30.
19. Kuznetsov Yu.A.: Elements of Applied Bifurcation Theory (3d Edition). Springer, 2004, 632p.
20. Borisov A.V., Kozlov V.V., Mamaev I.S. On the fall of a heavy rigid body in an ideal fluid //Proceedings of the Steklov Institute of Mathematics. 2006. Vol. 253. No 1. P. S24-S47.
21. Borisov A. V., Mamaev I. S. On the motion of a heavy rigid body in an ideal fluid with circulation //Chaos: An Interdisciplinary Journal of Nonlinear Science, 2006, vol. 16, no. 1, 013118.
22. Kozlov V.V. On the problem of fall of a rigid body in a resisting medium //Vestnik Moskov. Univ. Ser. I Mat. Mekh. 1990. No 1. P. 79-86.
23. Tanabe Y., Kaneko K. Behavior of a Falling Paper //Phys. Rev. Lett., 1994, vol. 73, pp. 1372-1375.
24. Mahadevan L., Aref H., Jones S.W. //Comment on “Behavior of a Falling Paper”. Phys. Rev. Lett. , 1995, vol.75, p.1420.
25. Tanabe Y., Kaneko K. Tanabe and Kaneko Reply //Phys. Rev. Lett. , 1995, 75, p.1421.
26. Mahadevan L. Tumbling of a falling card //C. R. Acad. Sci. Paris, Ser. II b, 1996, vol. 323, pp.729-736.
27. Belmonte A., Eisenberg H., Moses E. From Flutter to Tumble: Inertial Drag and Froude Similarity in Falling Paper //Phys. Rev. Lett., 1998, vol. 81, no 2, pp. 345-348.
28. Andersen A., Pesavento U., Wang Z. J. Analysis of transitions between fluttering, tumbling and steady descent of falling cards //J. Fluid Mech., 2005, vol. 541, pp. 91-104.
29. Pesavento U., Wang Z. J. Falling paper: Navier-Stokes solutions, model of fluid forces, and center of mass elevation //Phys. Rev. Lett., 2004, vol. 93, no. 14, 144501.
30. Andersen A., Pesavento U., Wang Z. J. Unsteady aerodynamics of fluttering and tumbling plates //Journal of Fluid Mechanics, 2005, vol. 541, pp. 65-90.
31. Noor D. Z., Chern M. J., Horng T. L. Study of a Freely Falling Ellipse with a Variety of Aspect Ratios and Initial Angles. The 22nd International Conference on Parallel Computational Fluid Dynamics, 2010: http://www1.math.fcu.edu.tw/~tlhorng/paper/Extended_abstract.pdf
32. Caetano V. F. R. Calculation of the dynamic behavior of a falling plate or disk in a fluid. – 2010: https://fenix.tecnico.ulisboa.pt/downloadFile/395142133553/resumo.pdf
33. Dupleich, P. Rotation in Free Fall of Rectangular Wings of Elongated Shape. UNT Digital Library. http://digital.library.unt.edu/ark:/67531/metadc64688/
34. Huang W., Liu H., Wang F., Wu J., Zhang H.P. Experimental study of a freely falling plate with an inhomogeneous mass distribution //Phys. Rev. E., 2013, vol. 88, no. 5, 053008.
35. Mahadevan L., Ryu W. S., Samuel A. D. T. Tumbling cards //Physics of Fluids (1994-present), 1999, vol. 11, no. 1, pp. 1-3.
36. Field S.B., Klaus M., Moore M.G., Nori F. Chaotic dynamics of falling disks //Nature, 1997, vol. 388, no. 6639, pp. 252-254.
37. Heisinger L., Newton P., Kanso E. Coins falling in water //Journal of Fluid Mechanics, 2014, vol. 742, pp. 243-253.
38. Leweke T., Thompson M. C., Hourigan K. Motion of a Möbius band in free fall //Journal of Fluids and Structures, 2009, vol. 25, no 4, pp. 687-696.
39. Lugt H.J. Autorotation //Annual Review of Fluid Mechanics, 1983, vol. 15, no. 1, pp. 123-147.

40. Paoletti P., Mahadevan L. Planar controlled gliding, tumbling and descent //Journal of Fluid Mechanics, 2011, vol. 689, pp. 489-516.
41. Ramodanov S. M., Tenenev V. A., Motion of a body with variable distribution of mass in a boundless viscous liquid, Rus. J. Nonlin. Dyn., 2011, Vol. 7, No. 3, pp. 635-647
42. Fernandes A.C., Sefat S.M. Bifurcation from Fluttering to Autorotation of a Hinged Vertical Flat Plate Submitted to a Uniform Current. Proceedings of the 11th International Conference on the Stability of Ships and Ocean Vehicles, 23-28 September 2012, Athens, Greece, pp.1-12.
43. Michelin S., Smith S.G.L. Falling cards and flapping flags: understanding fluid–solid interactions using an unsteady point vortex model //Theoretical and Computational Fluid Dynamics, 2010, vol. 24, no. 1-4, pp. 195-200.
44. Andronov, A.A., Vitt, A.A., Khaĭkin, S.Ė.: Theory of oscillators. Pergamon Press: Oxford, 1966. 848p.
45. Butenin N.V., Nejmark Y.I. and Fufaev N.A. An Introduction to the Theory of Nonlinear Oscillations. Nauka: Moscow, 1987. 382p.
46. Lorenz E.N. Deterministic nonperiodic flow //Journal of the atmospheric sciences. 1963. Vol. 20. No 2. P. 130-141.
47. Sparrow C. The Lorenz equations: bifurcations, chaos, and strange attractors. New York: Springer-Verlag, 1982, 269p.
48. Shilnikov L. Mathematical problems of nonlinear dynamics: a tutorial //Journal of the Franklin Institute, 1997, vol. 334, no. 5, pp. 793-864.
49. Tucker W. A rigorous ODE solver and Smale's 14th problem //Foundations of Computational Mathematics, 2002, vol. 2, no. 1, pp. 53-117.
50. Pikovski A.S., Rabinovich M.I., Trakhtengerts V.Y. Appearance of chaos at decay saturation of parametric instability //Sov. Phys. JETP. 1978. Vol. 47. P. 715-719.
51. Hénon M. On the numerical computation of Poincaré maps //Physica D, 1982, vol. **5**, pp. 412–414.
52. Swift J. W., Wiesenfeld K. Suppression of period doubling in symmetric systems //Phys. Rev. Lett., 1984, vol. 52, no. 9, pp. 705-708.
53. Magnus K., Popp K. Schwingungen. Stuttgart: Teubner, 1961. 405p.
54. Feigenbaum M.J. Quantitative universality for a class of nonlinear transformations //Journal of statistical physics, 1978, vol. 19, no. 1. pp. 25-52.
55. Feigenbaum M. J. Universal behavior in nonlinear systems //Physica D: Nonlinear Phenomena. 1983. Vol. 7. No 1. P. 16-39.